Structural insights into pseudokinase domains of receptor tyrosine kinases

Joshua B. Sheetz[1,2,9], **Sebastian Mathea**[3,4,5,9], **Hanna Karvonen**[6,9], **Ketan Malhotra**[1,2,10], **Deep Chatterjee**[3,4], **Wilhelmiina Niininen**[6], **Robert Perttilä**[6], **Franziska Preuss**[3,4], **Krishna Suresh**[7], **Steven E. Stayrook**[1,2], **Yuko Tsutsui**[1,2], **Ravi Radhakrishnan**[7], **Daniela Ungureanu**[6,8,*], **Stefan Knapp**[3,4,5,*], **Mark A. Lemmon**[1,2,11,*]

[1]Department of Pharmacology, Yale University School of Medicine, New Haven, CT 06520, USA.
[2]Yale Cancer Biology Institute, Yale University West Campus, West Haven, CT 06516, USA.
[3]Institute for Pharmaceutical Chemistry, Johann Wolfgang Goethe-University, D-60438 Frankfurt am Main, Germany [4]Buchmann Institute for Molecular Life Sciences, Structural Genomics Consortium, D-60438 Frankfurt am Main, Germany [5]German Cancer Consortium DKTK Frankfurt/Mainz, D-60438 Frankfurt, Germany [6]Cancer Signaling, Faculty of Medicine and Health Technology and BioMediTech, Tampere University, Tampere, 33014, Finland. [7]Department of Bioengineering, University of Pennsylvania, Philadelphia, PA 19104, USA. [8]Genome-Scale Biology, Research Programs Unit, University of Helsinki, FI-00014, Helsinki, Finland [9]These authors contributed equally [10]Present address: MRC Laboratory of Molecular Biology, Cambridge Biomedical Campus, Cambridge CB2 0QH, UK. [11]Lead contact

SUMMARY

Despite their apparent lack of catalytic activity, pseudokinases are essential signaling molecules. Here, we describe the structural and dynamic properties of pseudokinase domains from the Wnt-binding receptor tyrosine kinases (PTK7, ROR1, ROR2, RYK), which play important roles in development. We determined structures of all pseudokinase domains in this family, and found that they share a conserved inactive conformation in their activation loop that resembles the autoinhibited insulin receptor kinase (IRK). They also have inaccessible ATP binding pockets, occluded by aromatic residues that mimic a cofactor-bound state. Structural comparisons revealed

SUPPLEMENTAL INFORMATION
Supplemental information includes seven figures and two tables, and can be found in the online version of this article.

significant domain plasticity, and alternative interactions that substitute for absent conserved motifs. The pseudokinases also showed strikingly similar dynamic properties to IRK. Despite the inaccessible ATP site, screening identified ATP competitive typeII inhibitors for ROR1. Our results set the stage for an emerging therapeutic modality of "conformational disruptors" to inhibit or modulate non-catalytic functions of pseudokinases deregulated in disease.

eTOC Blurb

Sheetz et al. ask how Wnt-binding receptor tyrosine kinases can signal through intracellular 'pseudokinase' domains. They find that these domains resemble autoinhibited kinases, but are dynamic enough to regulate signaling through conformational switching. They find small molecules that can alter pseudokinase conformation, suggesting routes for modulating this receptor class therapeutically.

Graphical Abstract
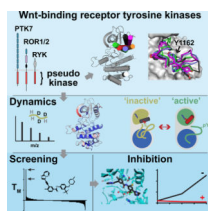
Keywords

Receptor tyrosine kinases; pseudokinases; Wnt signaling; growth factor signaling; protein conformation; targeted therapies; ponatinib; GZD824; cancer

---

INTRODUCTION

As receptor tyrosine kinase (RTK) signaling mechanisms have become increasingly well understood (Lemmon and Schlessinger, 2010), those mediated by the subset of RTKs thought to lack kinase activity remain largely enigmatic (Manning et al., 2002; Mendrola et al., 2013). Approximately 10% of the >500 predicted human protein kinases are classed as pseudokinases, assumed to lack phosphotransferase activity because of substitutions of conserved and essential catalytic residues (Boudeau et al., 2006; Manning et al., 2002). Five of the 58 human RTKs fall into this category: ErbB3/HER3, protein tyrosine kinase 7 (PTK7)/colon carcinoma kinase 4 (CCK4), EphB6, EphA10, and SuRTK106 (which lacks an extracellular region and was not included in our study). Three additional RTKs (ROR1, ROR2 and RYK) have substitutions in conserved motifs and lack both kinase activity (Debebe and Rathmell, 2015; Gentile et al., 2011; Katso et al., 1999) and ATP binding (Murphy et al., 2014). These 'RTK pseudokinases' are depicted in Fig. 1A, and the pseudokinase domain sequences are compared in Fig. S1.

Beyond the basic question of how RTKs can signal without kinase activity, strong links of RTK pseudokinases to disease have prompted significant interest in developing therapeutic approaches to inhibit their signaling functions (Bailey et al., 2015; Kung and Jura, 2019).

ErbB3 is associated with lung, colon, gastric, and other cancers (Amin et al., 2010; Jaiswal et al., 2013), especially in resistance to inhibitors of other EGFR family members. PTK7, ROR1/2, and RYK are all involved in Wnt signaling (Green et al., 2014; Karvonen et al., 2018; Peradziryi et al., 2012), and elevation of their expression is associated with cancer development and metastasis in several hematological and solid tumors (Debebe and Rathmell, 2015; Karvonen et al., 2018). EphB6 and EphA10 are also reported to play important roles in tumorigenesis (Liang et al., 2019; Nagano et al., 2014). Antibodies targeting the ErbB3 extracellular region are in clinical development for several solid tumors (Jacob et al., 2018). ROR1 antibodies are being tested clinically in chronic lymphocytic leukemia (CLL) and other cancers (Choi et al., 2018; Choi et al., 2015), as is a small molecule claimed to target the ROR1 extracellular region (Liu et al., 2019). PTK7 is also the target of an antibody-drug conjugate in clinical development (Damelin et al., 2017; Katoh, 2017). No validated pharmacological agents that target intracellular regions of RTK pseudokinases have been described, however – largely because their mechanistic role in signaling is poorly understood.

The nucleotide binding properties of RTK pseudokinase domains vary. Those from PTK7, ROR1/2, and RYK all fail to bind ATP (Murphy et al., 2014), whereas those from ErbB3 and EphB6 bind ATP quite strongly (Jura et al., 2009; Murphy et al., 2014; Shi et al., 2010). ErbB3 also displays low level kinase activity (Shi et al., 2010; Steinkamp et al., 2014), inhibition of which does not block signaling (Novotny et al., 2016; Shi, 2012). Without phosphotransferase activity, pseudokinases are thought to signal by allosterically regulating binding partners (Zeqiraj and van Aalten, 2010). To help understand this role, we combined crystallographic, biophysical, and chemical biology studies. We show that RTK pseudokinase domains adopt structures closely related to the inactive state of their closest kinase-active homologue, and with comparable dynamics – suggesting a similar propensity for conformational changes. We also demonstrate that a pseudokinase domain that fails to bind ATP can nonetheless be targeted with small molecules that bind its vestigial ATP-binding site. The insight provided here into the structure and dynamics of pseudokinase domains suggests approaches for defining the mechanisms of their function and for targeting them pharmacologically.

RESULTS AND DISCUSSION

As a first step, we aimed to establish a comprehensive structural description of RTK pseudokinases – adding to structures of the ErbB3 (Jura et al., 2009; Shi et al., 2010) and ROR2 (Artim et al., 2012) pseudokinase domains. We determined crystal structures of pseudokinases from the remainder of the Wnt-binding RTK (PTK7/ROR/RYK) family, and also modeled the Eph RTK pseudokinases.

The activation loops of PTK7, ROR, and RYK pseudokinase domains mimic autoinhibitory interactions seen in inactive IRK

We determined crystal structures of the PTK7 and RYK pseudokinase domains (to 1.95 Å and 2.38 Å respectively) plus that of ROR1 bound to a small molecule (described in a later section), as summarized in Table 1. These pseudokinase domains all contain a YxxxYY

motif (or its vestiges) in the activation loop, similar to that in the insulin receptor kinase domain (IRK). The activation loop conformations also closely resemble that of inactive, autoinhibited, IRK (Fig. 1B) – immediately raising the question as to what activity or property is 'autoinhibited' in the pseudokinases. Inactive IRK is autoinhibited by simultaneous projection of a key tyrosine side chain (Y1162) into the protein substrate-binding site and occlusion of the ATP-binding site by the IRK DFG motif (Hubbard et al., 1994). The PTK7, RYK, and ROR pseudokinases all similarly place a tyrosine in precisely the same location as Y1162 of IRK (Fig. 1B), and the YxxxYY motif configuration (FxxxYH in RYK) is highly conserved. By contrast, the ErbB3 activation loop adopts a different conformation – instead resembling the inactive EGFR kinase domain (Jura et al., 2009; Shi et al., 2010). ErbB3 does place its single activation loop tyrosine (Y848; not conserved in EGFR) in a very similar location to Y1162 in IRK, however (Littlefield et al., 2014), suggesting that projecting an activation loop tyrosine into the (protein) substrate binding site may be common across RTK pseudokinases (Fig. 1C).

The ATP-binding site of inactive IRK is occluded in two ways (Hubbard et al., 1994). First, the side-chain of the DFG phenylalanine (F1151) projects into the adenine ring binding site (Fig. 1D: IRK inactive). Second, the main chain following the DFG motif occludes the binding site for the ATP β- and γ-phosphate groups (Fig. 1D). This is the 'DFG-out' conformation (Huse and Kuriyan, 2002; Modi and Dunbrack, 2019), frequently seen in inactive kinases – in which the aspartate side-chain (D1150) is also oriented away from the active site so that is cannot coordinate Mg^{2+}. In active kinases, the DFG motif instead adopts an 'in' conformation, allowing Mg^{2+} coordination and repositioning the phenylalanine side-chain to allow ATP binding and to complete the so-called regulatory spine (Fig. S2) or 'R-spine' (Kornev and Taylor, 2010). The Wnt-binding RTK pseudokinases all have an altered DFG motif ('ALG' in PTK7, 'DLG' in the RORs and 'DNA' in RYK; Fig. 1D). The conformation of this altered motif is always closer to 'DFG-out' than 'DFG-in' (Fig. 1D). As a result, each R-spine is broken (Fig. S2) – although in a different way for RYK than for PTK7 or ROR2 (which more closely resemble inactive IRK). Moreover, the leucine side-chains in the PTK7 'ALG' motif (L949) and the ROR2 'DLG' motif (L634) occlude the ATP-binding site (Fig. 1D). RYK is an exception, as its 'DNA' motif lacks a corresponding hydrophobic side-chain – although the main chain after this motif passes through (and occludes) the β/γ phosphate group-binding region (Fig. 1D). In contrast with the Wnt pseudokinase RTKs, the ErbB3 DFG motif adopts an 'in' conformation that completes the R-spine and leaves the ATP-binding site open to allow nucleotide binding (Figs. 1D and S2).

Aromatic side-chains from the hinge region occlude the PTK7, ROR, and RYK ATP-binding sites

ATP binding to PTK7 and ROR2 is prevented by projection of a tyrosine side-chain from the $\beta5/\alpha D$ hinge region (Y877 and Y555 respectively) into the adenine ring binding site (Fig. 1D). This position is two residues C-terminal to the gatekeeper, and is a tyrosine in ~50% of tyrosine kinases – although replaced by leucine (L1078) in IRK. The side-chain at this position typically projects away from the ATP binding site (as for L1078 in IRK and Y770 in ErbB3; Fig. 1D). The alternative side-chain orientation in PTK7 and ROR2 results from a rotation of their N-lobes about the $\beta5/\alpha D$ hinge (Fig. S3A,B). RYK does not undergo this N-

lobe rotation (Fig. S3C), allowing its corresponding tyrosine (Y413) to adopt the canonical orientation (Fig. 1D). The RYK adenine ring binding site is instead occluded by the side-chain of a phenylalanine (F362) in the altered β3 VAIK motif (AFVK in RYK). A leucine at this position in PTK7 (L828 in its VLVK variant of the VAIK motif) also contributes to ATP-binding site occlusion.

Whereas the ATP binding sites in RTK pseudokinases are occluded by side-chains from multiple motifs, the IRK ATP-binding site is only obstructed by its DFG motif (Figs. 1D and S4A), suggesting that simply flipping the DFG motif from 'out' to 'in' might allow ATP binding. Indeed, IRK can bind Mg^{2+}-ATP without activation loop phosphorylation (Till et al., 2001) as can be seen using differential scanning fluorimetry (DSF). DSF monitors the influence of ligand binding on the melting temperature (T_M) of a protein, as reported by increased fluorescence of SYPRO Orange as it binds to thermally unfolded protein (Fedorov et al., 2012). Binding of Mg^{2+}-ATP to unphosphorylated IRK destabilized the kinase domain by ~3.5°C (Fig. S4B) – rather than stabilizing – which may reflect disruption of the autoinhibitory activation loop interactions described above. In contrast to IRK, the PTK7, ROR1, ROR2, and RYK pseudokinase domains showed no significant stability change upon adding 5 mM Mg^{2+}-ATP (Fig. S4B), suggesting no binding, in agreement with previous work (Murphy et al., 2014). Moreover, a D644A mutation in ROR2 (equivalent to D1161A in IRK, which promotes ATP binding) failed to restore ATP binding.

Another important difference between IRK and the Wnt-binding RTK pseudokinases is revealed by comparing their catalytic spines ('C-spines'). The 'C-spine' is a non-contiguous hydrophobic motif defined by Kornev and Taylor (Kornev and Taylor, 2010). In ATP-bound active kinases, it is completed by the adenine ring of bound ATP, as seen in PKA and active IRK in Fig. S2. In an inactive kinase, by contrast, the C-spine is broken (see inactive IRK in Fig. S2) and the side-chain of the DFG-motif phenylalanine (from the R-spine) projects into the gap. Interestingly, the C-spine is fully contiguous in PTK7, ROR2 and RYK despite no direct contribution from R-spine (DFG motif) residues or ATP (Fig. S2) – although the side-chain of the ALG/DLG motif leucine does abut the intact C-spine in PTK7 and ROR2.

PTK7, ROR, and RYK pseudokinases adopt different 'hybrid' conformations stabilized by unique sets of interactions

Although the PTK7, ROR, and RYK pseudokinase domains all closely resemble inactive IRK in their activation loop configurations (Fig. 1B), they vary substantially in αC helix position (Fig. 2A) and in other structural features, details of which can be described as follows.

PTK7: Although PTK7 appears autoinhibited by its activation loop (and hinge tyrosine), it has an active-like 'in' αC disposition (Fig. 2A). As a result, the distance between the side-chains of the conserved αC glutamate (E846) and the VAIK motif β3 lysine (K830) is just 2.7 Å. This allows the αC/β3 salt bridge – a hallmark of active kinases – to form (Fig. 2B), and places K830 so that it could support ATP binding if the ATP-binding site were not occluded. PTK7 thus adopts an unusual 'pseudo' active-like kinase domain conformation.

ROR2: The ROR2 αC helix adopts the 'out' position as in inactive IRK (Fig. 2A). The side-chains of the αC glutamate (E524) and β3 lysine (K507) are therefore too far apart (~5 Å) for the hallmark αC/β3 salt bridge of active kinases to form (Fig. 2C) – and the β3 lysine (K507) is >7 Å away from where the ATP phosphates would reside in a putative nucleotide-bound state (Artim et al., 2012). A hydrogen bond between D633 in the degenerated ROR2 DFG motif (DLG) and R528 in αC also connects these two motifs in an unusual way (Fig. 2C).

RYK: The RYK pseudokinase domain has several unique structural features. First, as in PTK7, its αC helix adopts an *active*-like 'in' position (Fig. 2A), apparently 'pushed' into this position by a 2.5-turn α-helix (αB) at the domain's amino-terminus (Fig. 2D). This arrangement is reminiscent of the EphB2 kinase domain (Wybenga-Groot et al., 2001) and involves intimate clustering of hydrophobic side-chains at the αB/αC interface (Fig. 2D, left). Surprisingly, although the conserved β3 lysine (K364) is retained in RYK's degenerated VAIK motif (AFVK), and αC is 'in', the αC/β3 salt bridge that is a hallmark of active kinases does not form in RYK (Fig. 2D, right). Instead, K364 forms a predicted salt-bridge (2.6 Å) with D483 in RYK's degenerated DFG (DNA) motif, and the αC glutamate (E381) is close (3.0 Å) to R488 in the activation loop (three residues C-terminal to the degenerated DFG motif). The absence of a large hydrophobic side-chain in RYK's degenerated DFG motif also appears to be compensated for by the positioning of F491 in the small helix C-terminal to this motif (Fig. S4A). In addition, the presence of a glutamine (Q337) in place of the first glycine of the glycine rich loop in RYK contributes to steric exclusion of RYK's ATP binding site (Fig. S4A).

Differences in Eph pseudokinase domain autoinhibition

To extend these comparisons across the RTK pseudokinases, we modeled the EphA10 and EphB6 pseudokinase domains, so far of unknown structure. Apart from EphA10 and EphB6, the remaining 12 human ephrin receptors (Ephs) are catalytically active (Liang et al., 2019). They are regulated by phosphorylation of key juxtamembrane (JM) tyrosines, which relieves intramolecular autoinhibition to allow *trans*-autophosphorylation of a conserved activation loop tyrosine (Hornbeck et al., 2015) that corresponds to Y1162 in IRK. EphA10 retains this conserved activation loop tyrosine, but not the regulatory JM tyrosines. Conversely, EphB6 retains the regulatory JM tyrosines but not the activation loop tyrosine (and has an unusually short activation loop). In the few published Eph kinase structures in inactive conformations (Dong et al., 2014; Kung et al., 2016; Overman et al., 2014), the activation loop tyrosine is ordered and projects into the substrate binding site like Y1162 of inactive IRK. Similarly, our EphA10 pseudokinase model, (based on EphB3; see STAR Methods) places this tyrosine (Y801) in the autoinhibitory location (Fig. 3A,B). Y801 simultaneously contacts the arginine close to the end of the catalytic loop (R774 in EphA10) and an adjacent EphA10-specific histidine (H775) – substituting for interaction with the (absent) HRD aspartate (Fig. 3B). This IRK-like docking of Y801 constrains the EphA10 activation loop so that the backbone of the DFG motif (GFG in EphA10) passes through and occludes the ATP-binding site as in IRK (Fig. 3C). No additional occlusion of the ATP-binding site from the β5/αD hinge is seen, suggesting that EphA10 shares IRK's ATP-binding properties.

EphB6 lacks 14 activation loop residues (including the conserved tyrosine), so cannot adopt the inactive-like conformation seen in IRK and EphA10. Instead, the shortened and unrestrained EphB6 activation loop adopts an active-like conformation in our models (Fig. 3), leaving EphB6 free to bind ATP as reported experimentally (Becher et al., 2013; Murphy et al., 2014) – with a possible positive contribution from R813 (Fig. 3C). Thus, whereas EphA10 seems to resemble IRK and the Wnt-binding RTK pseudokinases, EphB6 appears to resemble ErbB3 in having an unprotected ATP-binding site.

Pseudokinases and kinases display similar conformational dynamics

It has been hypothesized that pseudokinases function as allosteric regulators or scaffolding molecules in cell signaling (Kung and Jura, 2019; Reiterer et al., 2014; Zeqiraj and van Aalten, 2010), which might require dynamic transitions between different conformational states as seen for canonical kinases (Huse and Kuriyan, 2002; Kornev and Taylor, 2015). Alternatively, pseudokinase domains might be more static than other kinase domains, allowing them to serve as rigid scaffolds – a view suggested by the fully occluded ATP-binding sites, well-defined autoinhibitory activation loops, and additional intramolecular interactions seen in PTK7, ROR2 and RYK but not in other protein kinases. To distinguish between these possibilities, we used hydrogen-deuterium exchange coupled with mass spectrometry (HDX-MS) to compare exchange dynamics of the pseudokinase domains with those of unphosphorylated, inactive IRK.

IRK activation requires the unphosphorylated activation loop to explore multiple conformations. These fluctuations can transiently reverse autoinhibition so that Mg^{2+}-ATP and substrate tyrosine can bind (Hubbard, 2013) – and the kinase can *trans*-phosphorylate its neighbor in an insulin receptor dimer to promote signaling. HDX-MS studies of IRK (Fig. 4A) illustrate this dynamic conformational exploration, with backbone amide protons in the YxxxYY motif-containing activation loop becoming almost completely exchanged within ~1 minute. Other regions of IRK are also quite dynamic, whereas the HRD motif (which harbors the catalytic base aspartate) and the β5/αD hinge (between N- and C-lobes) show the slowest HDX rates (Fig. 4A,B; Table S1). A similar overall dynamic picture has been reported for other protein kinases studied by HDX-MS (Bunney et al., 2018; Hsu et al., 2008; Iacob et al., 2009; Loving and Underbakke, 2019; Shi et al., 2006; Sours et al., 2008; Tsutsui et al., 2016), so IRK appears typical.

Far from being more static than typical kinases, all of the pseudokinase domains studied here show very similar dynamic characteristics to IRK (Fig. 4C). Most importantly, the activation loops of the pseudokinase domains – which contain the DFG and YxxxYY motifs – all showed very similar HDX rates to those of IRK. The pseudokinases also share with IRK a relatively low rate of exchange in the HRD motif. Other general trends are also similar, although each pseudokinase does display some unique features, such as increased β2/β3 loop exchange in PTK7 and ROR2, and reduced exchange in αC peptides for all pseudokinases compared with IRK. Regions in the C-lobe (notably αF and beyond) show much more variability from domain to domain, likely owing to differences in helix and loop lengths. In Fig. 4D, differences between a mean 'exchangeability index' for the pseudokinase domains as a group (see STAR Methods) and HDX measured for IRK are

plotted on the IRK structure. For most of the structure, the difference is within two standard deviations of the mean for pseudokinases (white). Differences exceed 2σ only in αC and the glycine-rich (β1/ β2) loop – which both show slightly less exchange in the pseudokinases (colored darker grey). By contrast, the β5/αD loop (leading into αD) and helix αI both show slightly higher exchange in pseudokinases (colored orange).

These results demonstrate that structural elements in the RTK pseudokinase domains are not significantly more rigid than in catalytically active counterparts such as IRK. This in turn suggests that the pseudokinases may maintain conformational switching-based regulatory mechanisms seen with active kinases, which could control scaffolding functions in signaling.

The intracellular pseudokinase domain elicits signaling functions

A major challenge in studying the Wnt-binding RTK pseudokinases has been the availability of experimental contexts for structure/function analysis of signaling (Green et al., 2014; Karvonen et al., 2018). Moreover, some in vivo studies have led to inferences that the intracellular pseudokinase domains of Wnt-binding RTKs are not required for signaling (Green et al., 2014; Hayes et al., 2013; Inoue et al., 2004; Stricker et al., 2017) – although this likely reflects Wnt sequestration by the extracellular regions of the overexpressed constructs.

Using an approach frequently employed in studies of RTKs (Collins et al., 1988; Warmuth et al., 2007), we expressed ROR1, ROR2 and PTK7 in the interleukin-3 (IL3) dependent BaF3 murine pro-B cell line (Fig. S5A). Whereas parental BaF3 cells die following IL3 withdrawal, a significant number of those expressing ROR2 survived in the absence of IL3 (Fig. S5B), and those expressing PTK7 showed some improved survival, consistent with previous studies (Prebet et al., 2010). In addition, ROR1-expressing cells (Fig. 5A) ultimately achieved IL3 independent proliferation (Fig. 5B) – consistent with the contribution of ROR1 (but not ROR2) to CLL and other hematological malignancies (Daneshmanesh et al., 2013; Karvonen et al., 2018). Intriguingly, the ROR1-expressing cells also responded to Wnt5a stimulation with significant elevation of ERK, AKT, and SRC phosphorylation (Fig. 5C), whereas no such response was seen in parental BaF3 cells or with ROR2 (Fig. S5C). These findings are consistent with studies of ROR1 signaling in a lymphoblastic leukemia cell-line (Bicocca et al., 2012) as well as other reports (Karvonen et al., 2019; Yamaguchi et al., 2012; Zhang et al., 2019). To ask whether the intracellular pseudokinase domain of ROR1 is required for these responses, we expressed a form of ROR1 that lacks its entire intracellular region (ROR1 ICR). Despite strong expression (Fig. 5A), ROR1 ICR lacked the ability to promote IL3-independent proliferation of BaF3 cells or to support Wnt5a-induced ERK, AKT, and SRC activation (Fig. 5B,C). Mutating the YxxxYY motif in the ROR1 activation loop to FxxxFF also abolished the ability of ROR1 to support BaF3 cell proliferation, as did mutating the VAIK β3 lysine (K506) to alanine (Fig. 5D,E). These data argue that the intracellular region of ROR1 (and those of other RTK pseudokinases) can provide important signaling functions despite lacking phosphotransferase activity. We were unable to detect any residual kinase activity for ROR1 (Fig. S5D,E) – as also reported by others (Murphy et al., 2014). We therefore suggest that the mutations analyzed in Fig. 5 impair ROR1 signaling function by altering the

conformation of its pseudokinase domain. Given the status of ROR1 and the other RTK pseudokinases as therapeutic targets, these findings prompted us to investigate targeting them with small molecules that might similarly modulate conformation. Our goal is to identify small molecules that modulate the scaffolding and/or allosteric functions of pseudokinase domains by inducing conformational changes – following precedents set with the TYK2 (Wrobleski et al., 2019), STRAD (Zeqiraj et al., 2009) and KSR (Dhawan et al., 2016) pseudokinases, as well as catalytically active kinases such as Aurora A (Gustafson et al., 2014).

Selective small molecule binders of the ROR1 pseudokinase domain

To identify small molecules that bind the ROR1, ROR2, PTK7, and RYK pseudokinase domains, we again used DSF, screening a total of 1486 compounds from the published protein kinase inhibitor set and the FDA-approved drug set from Selleckchem (see Table S2). The cut-off value for identifying 'hits' was thermal stabilization of $\pm 2°C$ (Fig. 6A). Despite the relatively large and kinase inhibitor-focused screening set, we failed to identify any hits for PTK7, ROR2, or RYK. For ROR1, however, we identified two closely related inhibitors that significantly increased T_M – indicating strong binding. These were ponatinib (O'Hare et al., 2009), a multi-targeted kinase inhibitor approved by the FDA for chronic myeloid leukemia (CML) and Philadelphia chromosome-positive acute lymphoblastic leukemia (ALL), and GZD824 (Ren et al., 2013) – which is structurally related. Both are BCR-ABL inhibitors that retain the ability to inhibit T315I gatekeeper-mutated ABL. Ponatinib and GZD824 stabilized ROR1 by $4.1°C$ and $6.0°C$ respectively (Fig. 6A), but did not bind ROR2, RYK, or PTK7. The two inhibitors are typical type-II inhibitors that likely induce a particular DFG-out conformation. The compact nature of their alkyne linker (Fig. 6B) is key for binding to T315I-mutated ABL (it is interesting to note that ROR1 has a phenylalanine at the gatekeeper position). To validate ponatinib and GZD824 as 'hits', and to exclude the possibility that they simply interfere in the DSF assay, we measured T_M for the ROR1 pseudokinase domain at a series of GZD824 concentrations (Fig. 6C). The resulting curve showed clear saturation (at ~10 μM) and an IC_{50} value of ~1 μM (for a ROR1 concentration of 2 μM in the assay) – arguing that K_D is submicromolar. Using a cellular thermal shift assay or CETSA (Martinez Molina et al., 2013), we further showed that both ponatinib and GZD824 engage (and stabilize) full-length ROR1 in BaF3 cells when added at 10 μM (Fig. 6D,E). Maximum stabilization of ROR1 in these assays was achieved with ~2 μM GZD824 or ~5 μM ponatinib (Fig. S6). These data suggest that both inhibitors form stoichiometric complexes with ROR1. Moreover, the fact that neither compound binds detectably to the ROR2, PTK7, or RYK pseudokinase domains demonstrates clear selectivity within the Wnt pseudokinase family – although GZD824 and ponatinib are known to inhibit a range of other tyrosine kinases. Importantly, as discussed below, ROR1-dependent activation of ERK and AKT phosphorylation by Wnt5a is inhibited at the same concentrations of ponatinib and GZD824 that maximally stabilize ROR1 in cells.

Binding of ponatinib or GZD824 induces conformational changes in the ROR1 pseudokinase domain

To investigate whether binding of ponatinib or GZD824 to the ROR1 pseudokinase domain induces conformational changes, we again turned to HDX-MS. Adding excess ponatinib or

GZD824 to the ROR1 pseudokinase domain led to significant protection from exchange in peptides close to the putative ATP-binding site (Fig. 7A,B and Fig. S7A,B), demonstrating that the occluded ATP-binding site of ROR1 can still accommodate kinase inhibitor-like molecules (presumably with associated conformational changes). Binding of ponatinib or GZD824 caused significant HDX protection in helix αC, αE, the β5/αD hinge region, the HRD motif, and the DFG (DLG) motif at the beginning of the activation loop – all regions adjacent to the vestigial ATP-binding site. By contrast, several more remote peptides showed *increased* backbone amide exchange upon inhibitor binding (red in Figs. 7A and S7A,B), arguing that the inhibitors induce significant changes in the pseudokinase domain's conformation. Regions affected in this way (red bars in Fig. 7A) included peptides in the β1/β2 (glycine-rich) loop region, part of strand β3, and much of the ROR1 activation loop – where inhibitor binding increases HDX in an already quite dynamic region of ROR1 (e.g. Fig. 7B, peptide *iv*), arguing that it destabilizes autoinhibitory interactions.

Crystal structure of the ROR1 pseudokinase domain bound to ponatinib

To directly visualize the mode of inhibitor binding to this pseudokinase, we co-crystallized the ROR1 pseudokinase domain with ponatinib and determined a 1.94 Å crystal structure (Fig. 7C). The structure confirmed that ponatinib binds to the region corresponding to ROR1's ATP-binding site, contacting all of the sites protected in HDX studies. Ponatinib binds ROR1 with the same binding mode seen when it binds ABL (O'Hare et al., 2009), as shown in Fig. S7C. The narrow alkyne linker of ponatinib, key for allowing it to bind T315I-mutated ABL, abuts the bulky gatekeeper phenylalanine (F552) side-chain in ROR1 (Fig. 7C inset). The structure of the ponatinib-bound ROR1 pseudokinase domain is very similar to that for ROR2 (which does not bind ponatinib or GZD824 yet shares 68% sequence identity). The configuration of the ROR1 activation loop YxxxYY motif closely resembles that of ROR2, RYK, PTK7 and inactive IRK in the static crystallographic view, but our HDX data (Fig. 7A,B) argue that binding of ponatinib or GZD824 significantly increases its solvent accessibility and dynamics. Moreover, the C-terminal part of the activation loop – immediately following the YxxxYY motif – was disordered in the ROR1/ponatinib complex structure, suggesting that accommodating ponatinib partly disrupts autoinhibitory docking of the activation loop in this region.

Another ponatinib-induced conformational change is seen in the DFG motif (DLG in ROR1/2). Ponatinib restrains this motif in ROR1 so that the leucine side-chain is disordered and the DLG aspartate (D633) side-chain is displaced (by ponatinib's trifluoromethylphenyl group) towards H613 of the HRD motif (see Fig. 7C inset). This forces ROR1's DLG motif into the same conformation seen for the DFG motif in ponatinib-bound ABL (O'Hare et al., 2009) – typical of that in kinases bound to type-II inhibitors (Modi and Dunbrack, 2019).

The largest-scale difference between the structures of the ROR1/ponatinib complex and ROR2 (which does not bind ponatinib) is a rotation (~20°) of the entire N-lobe about an axis (yellow rod in Fig. 7D) nearly coincident with strand β4. Ponatinib appears to simultaneously 'push' on the left-hand side of the N-lobe (near β1 and the β5/αD hinge) and 'pull' on its right-hand side (near αC) to achieve this rotation. Ponatinib displaces the side-chain of the β5/αD hinge tyrosine (Y554 in ROR1, Y555 in ROR2) that occludes ROR2's

ATP-binding site, as indicated by the red arrow on the left of Fig. 7D – inserting its imidazo(1,2-b)pyridazine moiety into that pocket. At the same time, ponatinib (docked onto the C-lobe) associates intimately with helix αC of ROR1, through an interaction between the nitrogen of its amide linker and E523 in αC plus van der Waal's contacts with the (hydrophobic) side-chains of L526, M527, and L530 in αC. All the corresponding residues are solvent-exposed in ROR2 (E524, L527, R528, and L531). Importantly, an arginine at position 528 of ROR2 (replaced by M527 in ROR1 – which contacts ponatinib) likely explains why ponatinib binds only ROR1, and not ROR2. An arginine in this position would interfere with ponatinib/αC interactions.

Together with our HDX-MS studies, this comparison of the ponatinib-bound ROR1 and unliganded ROR2 pseudokinase domain structures reveals one way in which a kinase inhibitor-like small molecule binder can modulate the conformation of a pseudokinase domain. Many effectors and activators bind to the N-lobe region of other kinases that is the focus of the conformational changes described here (Jura et al., 2011). Any similar mode of interaction that ROR1 participates in will thus be significantly affected by ponatinib or GZD824 binding. Ponatinib and GZD824 may therefore serve as pharmacologically privileged potential starting points for developing selective small molecule ROR1 interactors that could induce sufficiently extensive conformational changes in the pseudokinase domain to impair scaffolding functions of ROR1 in disease. Although efforts to investigate the effects of these inhibitors on the ROR1-mediated signaling seen in Fig. 5C are currently confounded by the promiscuity of ponatinib and GZD824 as kinase inhibitors, both compounds clearly inhibit ROR1-dependent activation of ERK and AKT phosphorylation by Wnt5a (Fig. S7D) at concentrations that we know maximally stabilize the receptor in CETSA experiments (Fig. S6). Moreover, it is interesting to note that Bicocca et al. found that ponatinib robustly inhibits AKT phosphorylation in acute lymphoblastic leukemia cells (Bicocca et al., 2012), in which ROR1 also appears to signal to AKT and ERK.

CONCLUSIONS

Our structural and modeling studies argue that the inactive kinase domains of RTK pseudokinases nonetheless retain the autoinhibitory interactions seen in their kinase-active relatives – the Wnt-binding RTKs sharing that autoinhibitory YxxxYY activation loop motif conformation seen in inactive IRK. RTK pseudokinases all seem either to bind nucleotide (as in ErbB3 and EphB6) or to mimic an ATP-bound form (as in PTK7, ROR1/2 and RYK) – as reported for others (Hammaren et al., 2015; Scheeff et al., 2009). Which of these two classes they fall into appears to correlate with whether or not the ATP-binding site is occluded in the inactive conformation of their closest kinase-active homologues.

One important question that arises from our results is why the pseudokinases retain the autoinhibitory interactions seen in their kinase-active relatives. One hypothesis is that pseudokinase domains function as rigid scaffolds, and the autoinhibitory interactions could promote rigidity (Kornev and Taylor, 2009; Murphy et al., 2014; Patel et al., 2017; Scheeff et al., 2009). On the contrary, our HDX-MS data argue that the PTK7, ROR, and RYK pseudokinase domains all display similar conformational dynamics to IRK, despite mimicking an ATP-bound state. It is well known that canonical protein kinases such as IRK

undergo transitions between active and (family-specific) inactive conformations (Huse and Kuriyan, 2002). The RTK pseudokinases are likely to have similar capabilities, providing a possible mechanism for controlling their ability to interact with binding partners and thus regulate signaling (Jacobsen and Murphy, 2017; Kung and Jura, 2019). In IRK, the inactive-to-active conformational transition is promoted by tyrosine phosphorylation of the activation loop YxxxYY motif (Hubbard, 2013). YxxxYY motif tyrosine phosphorylation has been reported for both PTK7 and ROR2 (Hornbeck et al., 2015), and could promote structural changes similar to those seen in IRK activation. Indeed, phosphorylation of the ROR1 and ROR2 pseudokinase domains has been suggested to be mediated by SRC recruitment (Akbarzadeh et al., 2008; Gentile et al., 2014). A related phosphorylation-dependent mechanism has also been described for the pseudokinase MLKL (mixed lineage kinase domain-like protein), where phosphorylation of the pseudokinase domain induces conformational changes, which control intra- and intermolecular interactions that regulate necroptosis (Petrie et al., 2019). Thus, pseudokinases may not only be scaffolds that allosterically regulate active kinases, but may in fact be regulated as conformational switches.

As with catalytically competent kinases, the dynamic structural changes involved in pseudokinase function might also be modulated by small molecules that bind the ATP site and modulate inter- and/or intra-molecular interactions. It might be possible to exploit this therapeutically. Several small molecules that bind the ATP-binding site of pseudokinases have been reported (Dhawan et al., 2016; Kung and Jura, 2019). For example, BMS-986165, an ATP-competitive inhibitor that binds the pseudokinase domain of TYK2 (a JAK family member) is effective in several murine models of autoimmune disease and is now in clinical testing (Wrobleski et al., 2019). JAK pseudokinase domains play important roles in regulating activity of their adjacent catalytically-competent (JH1) kinase domains, highlighted by frequent patient-derived JAK-activating mutations in the pseudokinase domain (Shan et al., 2014). In the case of TYK2, the unusual ATP site of its pseudokinase domain allowed selective inhibitor design that resulted in outstanding JAK isoform and kinome selectivity for BMS-986165 (Moslin et al., 2019; Wrobleski et al., 2019). Our findings support the value of similar concerted efforts to find small molecule modulators of the pseudokinase RTKs. Even if modulation of the properties of the pseudokinase domain by small molecules proves insufficient to block pseudokinase function, the ligands developed for the ATP-binding site of these proteins could instead be used for developing proteolysis targeting chimeras (PROTACs), as reported for both kinase-active RTKs (Burslem et al., 2018) and the RTK pseudokinase ErbB3 (Xie et al., 2014).

In conclusion, the results presented here demonstrate the feasibility of targeting the apparently inaccessible ATP site of ROR1 and related RTK pseudokinases. Given the important role of ROR1 and the other Wnt-binding RTKs in mediating growth signals, their selective targeting in this way represents a potentially valuable strategy for the development of future therapeutic agents.

STAR METHODS

RESOURCE AVAILABILITY

Lead contact for reagent and resource sharing—Further information and requests for resources and reagents should be directed to and will be fulfilled by the Lead Contact, Mark A. Lemmon (mark.lemmon@yale.edu).

Materials availability—Unique and stable reagents generated in this study are available upon request.

Data and code availability—PDB accession codes for the crystallographic coordinates and structure factors reported in this paper are: PDB: 6VG3 (PTK7 pseudokinase domain http://www.rcsb.org/structure/6VG3); PDB: 6TUA (RYK pseudokinase domain http://www.rcsb.org/structure/6TUA); PDB: 6TU9 (ROR1 pseudokinase domain with bound ponatinib http://www.rcsb.org/structure/6TU9). HDX-MS data and datapoints for all peptides are provided in Table S1 (Excel file). Results from the screen in Fig. 6A are provided in Table S2 (Excel file). Source code for determining 'exchangeability indices' in Fig. 4D is available at https://github.com/sheetzjb/RTKpseudokinases. Original gel data have been deposited to Mendeley Data: https://doi.org/10.17632/65v6bff7bm.1

EXPERIMENTAL MODEL DETAILS

Cell culture

Insect cells: *Spodoptera frugiperda* Sf9 cells were propagated at 27˚C with constant shaking at 120 rpm in serum-free ESF 921 Insect Cell Culture Medium (Expression Systems) containing 50 U/ml penicillin/streptomycin, and were used for production of all proteins except ROR$^{453-752}$ and RYK$^{292-607}$, for which the TriEx variant of Sf9 cells (EMD Millipore) were used – propagating at 27˚C with constant shaking at 90 rpm in serum-free Insect-XPRESS Medium (Lonza). All Sf9 cells were originally established from immature ovaries of female *S. frugiperda* pupae.

Mammalian cells: *Mus musculus* BaF3 cells (pro B cell line, DSMZ, ACC 300) were grown in RPMI media (Lonza, Basel, Switzerland) supplemented with 10% fetal bovine serum, 2 mM L-glutamine, 100 U/ml penicillin/streptomycin and 10% WEHI supernatant and incubated at 37˚C and 5% CO_2.

METHOD DETAILS

Plasmid construction for recombinant protein expression

Crystallization constructs: PCR was used to amplify DNA encoding residues 774–1069 of human PTK7, 453–752 of human ROR1 and 292–607 of human RYK. For PTK7 an N-terminal hexahistidine tag plus BamHI and HindIII restriction sites were included, and the fragment was subcloned into pFastBac1 (Invitrogen). For ROR1 and RYK, PCR fragments were inserted into the vector pFB-6HZB (Invitrogen) via ligation-independent cloning.

Hydrogen/Deuterium Exchange-Mass Spectrometry constructs: DNA fragments encoding residues 457–752 of human ROR1, 318–607 of human RYK (including a sequence

encoding an N-terminal TEV cleavage site), and 978–1283 of the human insulin receptor were amplified by PCR – to include sequence encoding an N-terminal hexahistidine tag and regions overlapping with the multiple cloning site of pFastbac1. Insert products and PCR-amplified pFastbac1 vector were digested with DpnI to remove template DNA, and were subsequently ligated using NEBuilder HiFi DNA Assembly Cloning Kit. A construct encoding residues 452–753 of human ROR2 was generated previously (Artim et al., 2012).

Protein production and purification

Protein production for crystallization: For expression of PTK7$^{774-1069}$, Sf9 cells at 2×10^6/ml were infected with recombinant baculovirus, and harvested by centrifugation after 3 days. Cells were lysed by sonication in Buffer A [500 ml of 20 mM Tris-HCl (pH 8.0), 300 mM NaCl, 10% (w/v) glycerol, 10 mM imidazole, 10 mM 2-mercaptoethanol, 1 mM PMSF, protease inhibitor cocktail (Roche)], and the lysate was clarified by centrifugation for 30 min at 16,000 rpm at 4˚C. Clarified lysate was then mixed with Ni-NTA (Ni^{2+}-nitrilotriacetate) beads (Qiagen) – pre-washed 3 times with Buffer A – for 1 h at 4˚C. Beads were then washed with 50 column volumes of Buffer A, and bound PTK7$^{774-1069}$ was eluted with increasing concentrations of imidazole in Buffer B (Buffer A + 400 mM imidazole). Eluted protein was further purified using a Fractogel TMAE (trimethylaminoethyl) anion-exchange column (EMD) equilibrated with Buffer AEX [25 mM Tris-HCl (pH 8.3), 10 mM NaCl, 2 mM DTT (dithiothreitol)] followed by a Fractogel SO3$^-$ cation exchange column (EMD) equilibrated with Buffer CEX [20 mM MES (pH 6.0), 150 mM NaCl, 2 mM DTT]. PTK7$^{774-1069}$ was eluted with a gradient from the starting NaCl concentration in the AEX/CEX column buffers to 1 M NaCl. Protein was then subjected to a final step of size-exclusion chromatography using a Superdex 75 10/300 column (GE Healthcare) equilibrated in 20 mM HEPES (pH 7.0), 150 mM NaCl, and 2 mM DTT.

For expressing ROR1 and RYK pseudokinase domains, exponentially growing TriEx cells (2×10^6/ml) were infected 1:64 with virus stock, incubated for 66 h at 27˚C with constant shaking, and harvested by centrifugation. Cells were resuspended in lysis buffer (50 mM HEPES pH 7.4, 500 mM NaCl, 20 mM imidazole, 0.5 mM TCEP, 5% glycerol) and lysed by sonication. Lysate was cleared by centrifugation and loaded onto a Ni NTA column. After washing with lysis buffer, the His6-tagged proteins were eluted in lysis buffer containing 300 mM imidazole. N-terminal tags were cleaved using TEV protease during a dialysis step (to remove imidazole). Contaminating proteins, the cleaved tags and TEV protease were then removed with a second Ni-NTA step. Finally, proteins were concentrated and subjected to size exclusion using an S200 16/600 column (GE Healthcare), from which ROR1 and RYK eluted as expected for monomers. Final yields were 2.5 mg/l insect cell medium (ROR1) and 0.4 mg/l insect cell medium (RYK). *Protein production for HDX-MS:* For production of ROR1$^{457-752}$, ROR2$^{452-753}$, or RYK$^{318-607}$, Sf9 cells were lysed by sonication in Buffer A [500 ml of 50 mM Tris-HCl (pH 8.0), 300 mM NaCl, 10 mM 2-mercaptoethanol, 1 mM PMSF, protease inhibitor cocktail (Roche)]. Lysate was clarified by centrifugation for 30 min at 16,000 rpm at 4˚C and loaded onto pre-washed a Ni-NTA (1 ml per liter of culture) for 1 h at 4˚C. Beads were then washed with 50 column volumes of Buffer A, and protein eluted with increasing concentrations of imidazole in Buffer B (Buffer A + 400 mM imidazole). Protein was next loaded onto a Fractogel TMAE

(trimethylaminoethyl) anion-exchange column (EMD) equilibrated with Buffer AEX [50 mM Tris-HCl (pH 8.0), 20 mM NaCl, 2 mM DTT (dithiothreitol)], and eluted with a NaCl gradient up to 1 M. Eluted fractions were diluted in Buffer CEX [50 mM MES (pH 6.0), 50 mM NaCl, 2 mM DTT] and loaded onto a Fractogel SO3⁻ cation exchange column (EMD) equilibrated with Buffer CEX, and eluted with a NaCl gradient in Buffer CEX up to 1 M. Protein was then subjected to size-exclusion chromatography using a Superdex 75 10/300 column (GE Healthcare) equilibrated in 20 mM HEPES (pH 7.0), 150 mM NaCl, and 100 μM TCEP [tris-(2-carboxyethyl)phosphine]. The PTK7 pseudokinase for HDX-MS was purified as described above for crystallization. Production of IRK$^{978-1283}$ followed the same procedure as for the RORs and RYK, except that Buffer A included 5% (w/v) glycerol, and the cation exchange step was omitted.

Crystallization—Crystals of PTK7$^{774-1069}$ were obtained using the hanging-drop vapor diffusion method, by mixing equal volumes of protein and reservoir solutions and equilibrating over the reservoir solution at 21˚C. The final protein concentration used was 10.5 mg/ml in 20 mM HEPES (pH 7.0), 150 mM NaCl, and 2 mM DTT. Crystals were obtained with a reservoir solution of 30% (w/v) PEG monomethyl ether 5,000, 100 mM ADA (pH 6.5), and 100 mM $(NH_4)_2SO_4$ (Jena Bioscience JBKinase Screen 3; condition D1).

Crystals of the RYK pseudokinase domain were also obtained using the sitting-drop vapor diffusion method, by transferring 130 nl drops of the RYK protein solutions at 11 mg/ml to a 3-well crystallization plate (Swissci) mixed with 70 nl precipitant solution (consisting of 100 mM HEPES (pH 7.5), 1.5 M Li_2SO4) and incubating at 20˚C. Crystals of the ROR1-ponatinib complex were obtained using the same method and volumes, but using 13 mg/ml ROR1 protein, 0.5 mM ponatinib, and a precipitant solution of 100 mM MES (pH 7.2), 12% (w/v) PEG 20K – and with incubation at 4˚C. Before flash-freezing in liquid nitrogen, PTK7 crystals were cryoprotected in reservoir solution containing 10% (w/v) glycerol, and RYK and ROR1-ponatinib crystals were cryoprotected in reservoir solution containing 25% ethylene glycol.

Structure determination—For PTK7, diffraction data were collected at beamline 23ID-C of GM/CA at Advanced Photon Source (APS) and were processed using HKL2000. PTK7 crystallized in space group *C222*$_1$ with three molecules in the asymmetric unit. Structures were solved by molecular replacement with Phaser, using co-ordinates for the MuSK TKD (PDB: 1LUF) as a search model (Till et al., 2002). Cycles of manual building/rebuilding using Coot (Emsley and Cowtan, 2004) were alternated with rounds of refinement using REFMAC (CCP4, 1994), plus composite omit maps calculated with CNS. PROCHECK identified no residues in the disallowed region of the Ramachandran plot. For RYK and ROR1/ponatinib, data were collected at Swiss Light Source (SLS) and analyzed, scaled and merged with Xia2 (Winter et al., 2013). Structures were solved by molecular replacement with Phaser using a ROR2 model (PDB: 4GT4) as a template for ROR1 (Artim et al., 2012) and an AXL model (PDB: 5TC0) as a template for RYK (Keung et al., 2017). The resulting models were refined with REFMAC5 (CCP4, 1994) and validated using MolProbity (Chen et al., 2010). Data collection and refinement statistics are listed in Table 1.

Hydrogen-Deuterium Exchange Mass Spectrometry (HDX-MS)—To obtain mass spectra of undeuterated and of D_2O-labelled peptides, purified protein ($IRK^{978-1283}$, $PTK7^{774-1069}$, $ROR1^{457-752}$, $ROR2^{452-753}$, or $RYK^{318-607}$) at 0.4 mg/ml in H_2O-based buffer (20 mM HEPES pH 7.4, 200 mM NaCl, 100 μM TCEP) was diluted twenty-fold with either H_2O-containing (undeuterated standards) or D_2O-containing (labeling conditions) buffer (20 mM HEPES pD 7.4, 200 mM NaCl, 100 μM TCEP using deuterium as solvent) to label amide hydrogen atoms (with final 95% D_2O concentration). Labeling was performed at 25°C for a range of times (10 s, 1 min, 10 min, 1 h, or 2 h), and the reaction was quenched by adding cold (4°C) 100 mM sodium phosphate buffer at pH 2.4, containing 2 M guanidine hydrochloride and 1% formic acid. For investigating the effect of GZD824 or ponatinib binding on ROR1, $ROR1^{457-752}$ (10 μM) was incubated with freshly prepared GZD824 or ponatinib at a final inhibitor concentration of 50 μM (and final DMSO concentration of 5% v/v) for 30 min at 25°C prior to deuterium labeling. The D_2O buffer contained 20 mM HEPES (pD 7.4), 200 mM NaCl, 50 μM GZD824 or ponatinib (and a final 5% DMSO), and the labeled sample was quenched by adding cold (4°C) 200 mM sodium phosphate buffer (pH 2.4) containing 2 M guanidine hydrochloride and 1% formic acid. Quenched samples were immediately injected onto a Waters HDX nanoAcquity UPLC (Waters, Milford, MA) with in-line digestion using an Enzymate BEH pepsin column (Waters, Milford, MA). Peptic fragments were trapped on an Acquity UPLC BEH C18 peptide trap and separated on an Acquity UPLC BEH C18 column. For IRK samples, a CSH C18 peptide trap and column were instead used for a more optimal peptide separation. A 7 min, 5–35% acetonitrile (0.1% Formic acid) gradient was used to elute peptides directly into a Waters Synapt G2-Si mass spectrometer in TOF mode – except for one biological replicate each of ROR1 unliganded, 5% DMSO, and 50 μM GZD824, which were collected using a Waters Xevo G2-XS QTOF mass spectrometer. MS^E data were acquired with a 15 to 30 V ramp CID for high energy acquisition of product ions as well as continuous lock mass (Leu-Enk) for mass accuracy correction. Peptide identification and protein sequence coverage maps were obtained from the undeuterated controls. Peptides were identified using the ProteinLynx Global SERVER 3.0.3 (PLGS) from Waters. Fully deuterated controls were performed by incubating in the presence of 2 M Guanidine-DCl for two hours prior to quenching (PTK7) or by incubating in D_2O buffer for 2–7 days (ROR1, ROR2, RYK, IRK). All deuterium labeling time points and controls were repeated three times. Data and statistical analyses were carried out as described previously (Houde et al., 2011). Briefly, the deuterium uptake by the identified peptic fragments through increasing deuteration time and for the fully deuterated control was determined using DynamX 3.0 (Waters). The normalized percentage of deuterium uptake at incubation time t ($\%D_t$) at an incubation time t for a given peptide was calculated as follows:

$$\%D_t = 100 * \frac{(m_t - m_0)}{(m_f - m_0)}$$

With m_t being the centroid mass at incubation time t, m_0 the centroid mass of the undeuterated control and m_f the centroid mass of the fully deuterated control. For studies of changes in ROR1 dynamics upon inhibitor binding, the percent deuteration difference plots $\%D_{exchange}$ (bound-unbound) presented in Fig. 7 were generated by subtracting the

corresponding percent deuteration at incubation time *t* calculated for the DMSO control (unbound) from that calculated with ponatinib or GZD824 (bound) thus:

$$\Delta\%D_{\text{exchange}} = \%D_{x,t}(bound) - \%D_{x,t}(unbound)$$

where *x* is each peptide, and *t* is the D_2O incubation time. A summary of the HDX-MS data collected and the HDX uptake data are included in Table S1 following consensus guidelines (Masson et al., 2019).

Differential scanning fluorimetry (DSF)—For thermal shift assays to study ATP binding in Fig. S4B, proteins were diluted in 20 mM HEPES (pH 7.5), 150 mM NaCl, and 100 μM TCEP to a final protein concentration of 5 μM. Nucleotide (5 mM) and/or $MgCl_2$ (10 mM) was added. SYPRO Orange (ThermoFisher Scientific) was then added (diluting 2500-fold into the sample), and 25 μl of the reaction mixtures were transferred to Concord 96-well polycarbonate PCR plates (Bio-Rad) with three technical replicates per condition. A Bio-Rad CFX96 Touch Real Time PCR machine was then used to monitor fluorescence at 530 nm while the temperature was raised by 1˚C per minute from 25˚C to 95˚C, with fluorescence measured at each increment. Fluorescence values were then plotted as a function of temperature after normalizing to the maximum fluorescence signal. Melting temperatures (T_M) were determined as the temperature at half-maximum fluorescence. Plots were generated using GraphPad Prism and represent the mean from three technical replicates.

For thermal shift assays used for small molecule screening (Fig. 6) and analysis of ponatinib binding (Fig. 6C), a 2 μM solution of the relevant purified pseudokinase domain in assay buffer (20 mM HEPES pH 7.4, 150 mM NaCl, 0.5 mM TCEP, 5% glycerol) was mixed 1:1000 with SYPRO Orange (Millipore Sigma). Test compounds were added to a final concentration of 10 μM (containing a final 2% DMSO). 20 μl of each sample were then placed in a 96-well plate, and the temperature increased stepwise from 25˚C to 95˚C. Fluorescence was monitored using a Mx3005P real-time PCR instrument (Stratagene) with excitation and emission filters set to 465 and 590 nm, respectively. Data were analyzed using MxPro software. Compound screening was performed as a single shot experiment. Potential pseudokinase binders were confirmed by repeating the experiment with an inhibitor concentration series (final concentrations up to 25 μM) – as seen for GZD824 in Fig. 6C. Plots were generated using GraphPad Prism and represent the mean from three technical replicates.

Small molecule screening—Small molecule screening was performed using the DSF assay described above. Our screening collection consisted of the kinase inhibitor library (#L1200 Selleckchem) and FDA-approved drug library (#L1300 Selleckchem), which includes a total of 1486 compounds. Failure to get hits with other pseudokinases does not simply reflect protein stability; the most stable Wnt-signaling pseudokinase was PTK7 (T_M ~ 59˚C) followed by RYK (54˚C), ROR1 (53˚C) and ROR2 (51˚C).

Homology models of EphA10 and EphB6—The crystal structure of EphB3 kinase (PDB: 3ZFY) in the inactive conformation (Overman et al., 2014) was selected as the template for modeling the inactive conformation of the EphA10 and EphB6 pseudokinase domains. After running BLAST for sequence alignment, the top crystal structure matches with EphA10 and EphB6 were found to be EphA4 (PDB: 2YGM) and EphB1 (PDB: 3ZFX) respectively, which were then used as templates for modeling active conformations of EphA10 and EphB6 pseudokinase domains. Coordinates of the active and inactive template kinases were downloaded from the Protein Data Bank, and missing residues were added by generating a homology model of the kinase using its own partial structure as the template. Five candidate models were generated from each of the templates by satisfying a set of static and dynamic spatial restraints in MODELLER. These restraints are expressed in terms of molecular probability density function, or objective function, which is optimized and applied in the ranking of the set of models constructed in MODELLER. The stereochemical quality of each model was further evaluated using the Discrete Optimized Protein Energy (DOPE) method – an atomic distance-dependent statistical potential optimized for model assessment in MODELLER, with the lowest DOPE score defining the preferred model. We structurally aligned all of the homology models for EphA10 and EphB6 to their template structures using Visual Molecular Dynamics (VMD), and generated Root Mean Square Deviation (RMSD) plots to find regions of variability. Most variation was seen in the first 50 residues for the homology models of the inactive structures of EphA10 and EphB6, so a hybrid approach was used to improve models for the inactive EphA10 and EphB6 conformations, where the coordinates for the first 50 residues came from the homology model for the active conformation of the kinase, and the rest of the coordinates come from the homology model for the inactive conformation. VMD was used to display structural models, and MODELLER was used for homology modeling of the pseudokinase domains for both EphA10 and EphB6.

BaF3 cell transfections—For expression in BaF3 cells, human ROR1, ROR2, PTK7 and RYK (or their truncated variants) were cloned into the pEFIRES-P vector (Hobbs et al., 1998) and electroporated into BaF3 cells using the 4D-Nucleofector X Kit L (Lonza) and a 4D Nucleofector X (Lonza), using program code DS-137. After 72 h, transfected cells were selected with increasing amounts of puromycin (0.5–1 μg/ml) for 2 weeks and tested for protein expression by Western blot (Figs. 5 and S5).

Cell viability and cell proliferation—Cell counts were determined by Trypan-blue exclusion using a Countess II automated cell counter (Life Technologies). Cell viability was measured using the CellTiter-Glow 2.0 Assay (CTG, Promega, Madison, USA) according to the manufacturer's instructions.

Western blotting—Whole cell lysates were prepared by lysing cells in ice cold NP-40 lysis buffer (50 mM Tris-HCl pH 7.4, 10% glycerol, 50 mM NaCl, 0.5% sodium deoxycholate, 1% NP-40, 20 mM NaF), supplemented with protease and phosphatase inhibitor cocktails (Bimake, Houston, TX, USA). Cell lysates were incubated 15 min on ice, clarified by centrifugation (4°C, 20 min, 20,000 x g), resuspended in $2 \times$ SDS sample buffer and boiled at 95°C for 5 min. Samples were separated by SDS-PAGE and transferred to

nitrocellulose membrane. Blots were blocked (4% BSA in 0.05% Tween 20 in 1×TBS) at RT for 1 h and incubated with primary antibody at 4˚C overnight. Blots were then washed 3 times with TBS/0.1% Tween 20 buffer, and subjected to secondary antibodies for 1 h at RT. Blots were scanned with an Odyssey® CLx Imaging System (LI-COR) and images analyzed using Image Studio Lite (LI-COR).

For Western blotting, the following antibodies were used: pAKT (S473, #6942), AKT (#9272), pERK1/2 (#9101), ERK1/2 (#4696), PTK7 (#25618), and SRC (#2109) from Cell Signaling Technology (Danvers, MA, USA); ROR1 4A5 (#564464) and ROR2 (#565550) from BD Biosciences (San Jose, CA, USA); anti-pTYR 4G10 (#05–321) from MerckMillipore; β-tubulin (#sc-166729) from Santa Cruz Biotechnology (Dallas, TX, USA); HA (#901513) from BioLegend (San Diego, CA). As secondary antibodies, IRDye® 800CW Donkey anti-Mouse IgG or IRDye® 680RD Donkey anti-Rabbit IgG (LI-COR, Lincoln, NE, USA) were used at 1:10.000 dilution.

Cellular thermal shift assay (CETSA)—CETSA was carried out according to the protocol described (Martinez Molina et al., 2013). Briefly, BaF3-ROR1 cells were treated with control (DMSO) or drug (10 μM) and incubated at 37˚C for 2 h. Cells were washed once and divided into aliquots with 0.5×10^6 cells each. Samples were heated (Bio-Rad T100TM Thermal Cycler) pairwise (control and drug-treated samples) for 3 min at 42–60˚C with 2˚C increments between pairs. After heating, cells were kept at room temperature for 3 min before transferring to ice. Cells were collected and lysed in Triton X100-containing lysis buffer (50 mM Tris-HCl, pH 7.5, 10% glycerol, 150 mM NaCl, 1 mM EDTA, 1% Triton X-100, 50 mM NaF) supplemented with protease and phosphatase inhibitor cocktails (Bimake, Houston, TX, USA), and were subsequently analyzed by SDS-PAGE and Western blotting using anti-HA (ROR1) and β-tubulin antibodies. Protein levels were quantified with Image Studio Lite (Li-COR) and normalized to 42˚C samples for both treatments.

in vitro kinase assays—Kinase assays were performed using either ATP hydrolysis as a readout (ADP-Glo) or fluorescence detection of phosphorylation of a peptide. For the ADP-Glo assay (Promega), a kit was used as recommended by the manufacturer. Briefly, reactions with 1 μM purified ROR1 pseudokinase domain or kinase controls (at 1 μM) were set up in kinase assay buffer (20 mM HEPES, pH 7.4, containing 10 mM MgCl₂, 0.02 mg/ml BSA, 0.1 mM Na₃VO₄, 2 mM DTT) with addition of 1 mM ATP and 0.1 mg/ml poly(Glu, Tyr) peptide substrate (Sigma-Aldrich). Reactions were incubated for 1 h at ambient temperature, and were then quenched by addition of an equal volume of ADP-Glo reagent – unreacted ATP was depleted over the course of 40 minutes at room temperature. An equal volume of detection reagent was then added to convert ADP in the reaction mixture into newly synthesized ATP, which serves as a substrate for the luciferase reaction. Samples were incubated for 1 h at room temperature before luminescence measurements were taken in a 384-well plate using a BioTek Synergy 2 Multi-Detection Microplate Reader. Experiments were performed in technical triplicate.

For fluorescent peptide assays, materials from Assay Quant Technologies were used as recommended by the manufacturer. Briefly, reactions with 1 μM purified ROR1 pseudokinase domain or kinase controls (at 1 μM) were set up in wells of a 384-well plate

with the final assay conditions: 50 mM HEPES, pH 7.5, containing 10 mM $MgCl_2$, 0.01% Brij-35, 0.1 mg/ml BSA, 1 mM ATP, and 20 µM peptide substrate sensor (AQT0001) that contains an incorporated Sox chromophore (Assay Quant). Reactions were incubated at 30°C for 2 h, and fluorescence intensities were collected every 2 min using a BioTek Synergy 2 Multi-Detection Microplate Reader. Experiments were performed in technical triplicate.

QUANTIFICATION AND STATISTICAL ANALYSIS

Structure determination and analysis—The statistical analysis of the structural models is provided in Table 1. Analysis of the molecular contacts and RMSD values were calculated using the CCP4 software package (CCP4, 1994).

Analysis of HDX dynamics—Raw MS^E mass spectra of undeuterated controls were used for peptide identification using ProteinLynx Global Server 3.0.3 (PLGS) from Waters. MS data from all controls and labeling conditions were then processed using DynamX to identify peptic peptides for each condition. All raw spectra for each peptide, labeling condition, drug condition, and charge state were then manually assessed for quality and for accurate peak assignment, at which point poor quality or incorrectly assigned peaks were unassigned. Average mass shifts of centroids and their standard deviations were then used to calculate percent uptake for each time point relative to a fully deuterated standard as described in Method Details. Uptake plots in Figs. 4A,C represent standard deviations from three independent labeling experiments for all conditions shown. Uptake plots in Fig. 7B represent mean ± SD from three independent protein preparations, for each of which three independent labelling experiments were performed in all conditions.

For 'exchangeability indices' (Fig. 4D), an R script was written to first calculate an average percent exchange for each residue in each pseudokinase (and IRK) at each time point. The value assigned to each residue was the mean (per residue) percent exchange seen for all peptides containing that residue. In parallel, each residue in each pseudokinase was assigned a corresponding homologous residue in IRK (based on sequence alignments). For the position corresponding to each residue in IRK, the mean (± SD) percent exchange was calculated across the 4 pseudokinases (ROR1, ROR2, RYK, PTK7) for each time point. This pseudokinase 'exchangeability index' value was then compared with the exchange value assigned to the corresponding residue in IRK – with deviations reported in terms of number of standard deviations (σ) away from the average pseudokinase uptake. Differences between pseudokinase exchangeability index and IRK exchange for each residue were averaged across all time points to depict areas that show more (orange) or less (black) HDX in pseudokinases than in IRK, as shown in Fig. 4D.

Western blot image processing—Raw images from the LI-COR Odyssey were imported in Adobe Photoshop, and linear contrast stretching was manually applied using the 'Levels' function – so that the darkest points of the images are black, and background is brought into the visible grey scale so that all features are registered.

Cell proliferation assays—All cell proliferation assays experiments were analyzed using Prism v8.0 software (GraphPad, San Diego, CA, USA). Cell proliferation data are represented as mean ± SD from four independent experiments each performed in technical triplicate. Statistical significance was determined using two-tailed *t*-tests. Two-sided p values were used to determine statistical significance, set as follows: *p 0.05, **p 0.01 and ***p 0.001.

Cellular thermal shift assays—All cellular thermal shift experiments were analyzed using Prism v8.0 software (GraphPad, San Diego, CA, USA). Individual bands were quantified using Image Studio Lite software and all values (band intensities) were normalized to unheated control sample (no inhibitor treatment) that denotes relative band intensity value of one. Standard deviation (SD) was calculated using three independent experiments. Curve fitting was done in Prism using Boltzmann sigmoidal algorithm. For concentration-dependent CETSA in Fig. S6, a constant heating temperature of 48°C was chosen based on the results from Fig. 6E. All values (band intensities) were normalized to heated samples without inhibitor. Curve fitting was done in Prism using one site (specific binding) algorithm.

Supplementary Material

Refer to Web version on PubMed Central for supplementary material.

ACKNOWLEDGMENTS

REFERENCES

Ablooglu AJ, Frankel M, Rusinova E, Ross JB, and Kohanski RA (2001). Multiple activation loop conformations and their regulatory properties in the insulin receptor's kinase domain. J. Biol. Chem. 276, 46933–46940. [PubMed: 11598120]

Adams PD, Afonine PV, Bunkoczi G, Chen VB, Davis IW, Echols N, Headd JJ, Hung LW, Kapral GJ, Grosse-Kunstleve RW, et al. (2010). PHENIX: a comprehensive Python-based system for macromolecular structure solution. Acta Crystallogr. D Biol. Crystallogr. 66, 213–221. [PubMed: 20124702]

Akbarzadeh S, Wheldon LM, Sweet SM, Talma S, Mardakheh FK, and Heath JK (2008). The deleted in brachydactyly B domain of ROR2 is required for receptor activation by recruitment of Src. PLoS One 3, e1873. [PubMed: 18365018]

Amin DN, Campbell MR, and Moasser MM (2010). The role of HER3, the unpretentious member of the HER family, in cancer biology and cancer therapeutics. Semin. Cell Dev. Biol. 21, 944–950. [PubMed: 20816829]

Artim SC, Mendrola JM, and Lemmon MA (2012). Assessing the range of kinase autoinhibition mechanisms in the insulin receptor family. Biochem. J. 448, 213–220. [PubMed: 22992069]

Bailey FP, Byrne DP, McSkimming D, Kannan N, and Eyers PA (2015). Going for broke: targeting the human cancer pseudokinome. Biochem. J. 465, 195–211. [PubMed: 25559089]

Becher I, Savitski MM, Savitski MF, Hopf C, Bantscheff M, and Drewes G. (2013). Affinity profiling of the cellular kinome for the nucleotide cofactors ATP, ADP, and GTP. ACS Chem. Biol. 8, 599–607. [PubMed: 23215245]

Bicocca VT, Chang BH, Masouleh BK, Muschen M, Loriaux MM, Druker BJ, and Tyner JW (2012). Crosstalk between ROR1 and the Pre-B cell receptor promotes survival of t(1;19) acute lymphoblastic leukemia. Cancer Cell 22, 656–667. [PubMed: 23153538]

Boudeau J, Miranda-Saavedra D, Barton GJ, and Alessi DR (2006). Emerging roles of pseudokinases. Trends Cell Biol. 16, 443–452. [PubMed: 16879967]

Bunney TD, Inglis AJ, Sanfelice D, Farrell B, Kerr CJ, Thompson GS, Masson GR, Thiyagarajan N, Svergun DI, Williams RL, et al. (2018). Disease variants of FGFR3 reveal molecular basis for the recognition and additional roles for Cdc37 in Hsp90 chaperone system. Structure 26, 446–458. [PubMed: 29478821]

Burslem GM, Smith BE, Lai AC, Jaime-Figueroa S, McQuaid DC, Bondeson DP, Toure M, Dong H, Qian Y, Wang J, et al. (2018). The advantages of targeted protein degradation over inhibition: An RTK case study. Cell Chem. Biol. 25, 67–77. [PubMed: 29129716]

CCP4 (1994). The CCP4 suite: Programs for protein crystallography. Acta Crystallogr. D Biol. Crystallogr. 50, 760–763. [PubMed: 15299374]

Chen VB, Arendall WB 3rd, Headd JJ, Keedy DA, Immormino RM, Kapral GJ, Murray LW, Richardson JS, and Richardson DC (2010). MolProbity: all-atom structure validation for macromolecular crystallography. Acta Crystallogr. D Biol. Crystallogr. 66, 12–21. [PubMed: 20057044]

Choi MY, Widhopf GF 2nd,, Ghia EM, Kidwell RL, Hasan MK, Yu J, Rassenti LZ, Chen L, Chen Y, Pittman E, et al. (2018). Phase I trial: Cirmtuzumab inhibits ROR1 signaling and stemness signatures in patients with chronic lymphocytic leukemia. Cell Stem Cell 22, 951–959. [PubMed: 29859176]

Choi MY, Widhopf GF 2nd,, Wu CC, Cui B, Lao F, Sadarangani A, Cavagnaro J, Prussak C, Carson DA, Jamieson C, et al. (2015). Pre-clinical specificity and safety of UC-961, a first-in-class monoclonal antibody targeting ROR1. Clin. Lymph. Myeloma Leuk. 15, S167–S169.

Collins MK, Downward J, Miyajima A, Maruyama K, Arai K, and Mulligan RC (1988). Transfer of functional EGF receptors to an IL3-dependent cell line. J. Cell. Physiol. 137, 293–298. [PubMed: 3263970]

Damelin M, Bankovich A, Bernstein J, Lucas J, Chen L, Williams S, Park A, Aguilar J, Ernstoff E, Charati M, et al. (2017). A PTK7-targeted antibody-drug conjugate reduces tumor-initiating cells and induces sustained tumor regressions c. Sci. Transl. Med. 9, eaag2611.

Daneshmanesh AH, Porwit A, Hojjat-Farsangi M, Jeddi-Tehrani M, Tamm KP, Grandér D, Lehmann S, Norin S, Shokri F, Rabbani H, et al. (2013). Orphan receptor tyrosine kinases ROR1 and ROR2 in hematological malignancies. Leuk. Lymphoma 54, 843–850. [PubMed: 22988987]

Debebe Z, and Rathmell WK (2015). Ror2 as a therapeutic target in cancer. Pharmacol. Ther. 150, 143–148. [PubMed: 25614331]

Dhawan NS, Scopton AP, and Dar AC (2016). Small molecule stabilization of the KSR inactive state antagonizes oncogenic Ras signalling. Nature 537, 112–116. [PubMed: 27556948]

Dong J, Zhao H, Zhou T, Spiliotopoulos D, Rajendran C, Li XD, Huang D, and Caflisch A. (2014). Structural analysis of the binding of type I, I1/2, and II inhibitors to Eph tyrosine kinases. ACS Med. Chem. Lett. 6, 79–83.

Emsley P, and Cowtan K. (2004). Coot: model-building tools for molecular graphics. Acta Crystallogr. D Biol. Crystallogr. 60, 2126–2132. [PubMed: 15572765]

Fedorov O, Niesen FH, and Knapp S. (2012). Kinase inhibitor selectivity profiling using differential scanning fluorimetry. Methods Mol. Biol. 795, 109–118. [PubMed: 21960218]

Gentile A, Lazzari L, Benvenuti S, Trusolino L, and Comoglio PM (2011). Ror1 is a pseudokinase that is crucial for Met-driven tumorigenesis. Cancer Res. 71, 3132–3141. [PubMed: 21487037]

Gentile A, Lazzari L, Benvenuti S, Trusolino L, and Comoglio PM (2014). The ROR1 pseudokinase diversifies signaling outputs in MET-addicted cancer cells. Int. J. Cancer 135, 2305–2316. [PubMed: 24706440]

Girdlestone C, and Hayward S. (2016). The DynDom3D Webserver for the analysis of domain movements in multimeric proteins. J. Comput. Biol. 23, 21–26. [PubMed: 26540459]

Green J, Nusse R, and van Amerongen R. (2014). The role of Ryk and Ror receptor tyrosine kinases in Wnt signal transduction. Cold Spring Harb. Perspect. Biol. 6, a009175. [PubMed: 24370848]

Gustafson WC, Meyerowitz JG, Nekritz EA, Chen J, Benes C, Charron E, Simonds EF, Seeger R, Matthay KK, Hertz NT, et al. (2014). Drugging MYCN through an allosteric transition in Aurora kinase A. Cancer Cell 26, 414–427. [PubMed: 25175806]

Hammaren HM, Ungureanu D, Grisouard J, Skoda RC, Hubbard SR, and Silvennoinen O. (2015). ATP binding to the pseudokinase domain of JAK2 is critical for pathogenic activation. Proc. Natl. Acad. Sci. U. S. A. 112, 4642–4647. [PubMed: 25825724]

Hayes M, Naito M, Daulat A, Angers S, and Ciruna B. (2013). Ptk7 promotes non-canonical Wnt/PCP-mediated morphogenesis and inhibits Wnt/β-catenin-dependent cell fate decisions during vertebrate development. Development 140, 1807–1818. [PubMed: 23533179]

Hobbs S, Jitrapakdee S, and Wallace JC (1998). Development of a bicistronic vector driven by the human polypeptide chain elongation factor 1alpha promoter for creation of stable mammalian cell lines that express very high levels of recombinant proteins. Biochem. Biophys. Res. Commun. 252, 368–372. [PubMed: 9826536]

Hornbeck PV, Zhang B, Murray B, Kornhauser JM, Latham V, and Skrzypek E. (2015). PhosphoSitePlus, 2014: mutations, PTMs and recalibrations. Nucleic Acids Res. 43(Database issue), D512–D520. [PubMed: 25514926]

Houde D, Berkowitz SA, and Engen JR (2011). The utility of hydrogen/deuterium exchange mass spectrometry in biopharmaceutical comparability studies. J. Pharm. Sci. 100, 2071–2086. [PubMed: 21491437]

Hsu YH, Johnson DA, and Traugh JA (2008). Analysis of conformational changes during activation of protein kinase Pak2 by amide hydrogen/deuterium exchange. J. Biol. Chem. 283, 36397–36405. [PubMed: 18984590]

Hubbard SR (2013). The insulin receptor: both a prototypical and atypical receptor tyrosine kinase. Cold Spring Harb. Perspect. Biol. 5, a008946.

Hubbard SR, Wei L, Ellis L, and Hendrickson WA (1994). Crystal structure of the tyrosine kinase domain of the human insulin receptor. Nature 372, 746–754. [PubMed: 7997262]

Hunter JD (2007). Matplotlib: A 2D graphics environment. Computing in Science and Engineering 9, 90–95.

Huse M, and Kuriyan J. (2002). The conformational plasticity of protein kinases. Cell 109, 275–282. [PubMed: 12015977]

Iacob RE, Pene-Dumitrescu T, Zhang J, Gray NS, Smithgall TE, and Engen JR (2009). Conformational disturbance in Abl kinase upon mutation and deregulation. Proc. Natl. Acad. Sci. U. S. A. 106, 1386–1391. [PubMed: 19164531]

Inoue T, Oz HS, Wiland D, Gharib S, Deshpande R, Hill RJ, Katz WS, and Sternberg PW (2004). C. elegans LIN-18 is a Ryk ortholog and functions in parallel to LIN-17/Frizzled in Wnt signaling. Cell 118, 795–806. [PubMed: 15369677]

Jacob W, James I, Hasmann M, and Weisser M. (2018). Clinical development of HER3-targeting monoclonal antibodies: Perils and progress. Cancer Treat. Rev. 68, 111–123. [PubMed: 29944978]

Jacobsen AV, and Murphy JM (2017). The secret life of kinases: insights into non-catalytic signalling functions from pseudokinases. Biochem. Soc. Trans. 45, 665–681. [PubMed: 28620028]

Jaiswal BS, Kljavin NM, Stawiski EW, Chan E, Parikh C, Durinck S, Chaudhuri S, Pujara K, Guillory J, Edgar KA, et al. (2013). Oncogenic ERBB3 mutations in human cancers. Cancer Cell 23, 603–617. [PubMed: 23680147]

Jura N, Shan Y, Cao X, Shaw DE, and Kuriyan J. (2009). Structural analysis of the catalytically inactive kinase domain of the human EGF receptor 3. Proc. Natl. Acad. Sci. U. S. A. 106, 21608–21613. [PubMed: 20007378]

Jura N, Zhang X, Endres NF, Seeliger MA, Schindler T, and Kuriyan J. (2011). Catalytic control in the EGF receptor and its connection to general kinase regulatory mechanisms. Mol. Cell 42, 9–22. [PubMed: 21474065]

Karvonen H, Barker H, Kaleva L, Niininen W, and Ungureanu D. (2019). Molecular mechanisms associated with ROR1-mediated drug resistance: Crosstalk with Hippo-YAP/TAZ and BMI-1 pathways. Cells 8, E812. [PubMed: 31382410]

Karvonen H, Perttilä R, Niininen W, Barker H, and Ungureanu D. (2018). Targeting Wnt signaling pseudokinases in hematological cancers. Eur. J. Haematol. 101, 457–465. [PubMed: 29989208]

Katoh M. (2017). Canonical and non-canonical WNT signaling in cancer stem cells and their niches: Cellular heterogeneity, omics reprogramming, targeted therapy and tumor plasticity Int. J. Oncol. 51, 1357–1369. [PubMed: 29048660]

Katso RM, Russell RB, and Ganesan TS (1999). Functional analysis of H-Ryk, an atypical member of the receptor tyrosine kinase family. Mol. Cell. Biol. 19, 6427–6240. [PubMed: 10454588]

Keung W, Boloor A, Brown J, Kiryanov A, Gangloff A, Lawson JD, Skene R, Hoffman I, Atienza J, Kahana J, et al. (2017). Structure-based optimization of 1H-imidazole-2-carboxamides as Axl kinase inhibitors utilizing a Mer mutant surrogate. Bioorg. Med. Chem. Lett. 27, 1099–1104. [PubMed: 28082036]

Kornev AP, and Taylor SS (2009). Pseudokinases: functional insights gleaned from structure. Structure 17, 5–7. [PubMed: 19141276]

Kornev AP, and Taylor SS (2010). Defining the conserved internal architecture of a protein kinase. Biochim. Biophys. Acta 1804, 440–444. [PubMed: 19879387]

Kornev AP, and Taylor SS (2015). Dynamics-driven allostery in protein kinases. Trends Biochem. Sci. 40, 628–647. [PubMed: 26481499]

Kung A, Chen YC, Schimpl M, Ni F, Zhu J, Turner M, Molina H, Overman R, and Zhang C. (2016). Development of specific, irreversible inhibitors for a receptor tyrosine kinase EphB3. J. Am. Chem. Soc. 138, 10554–10560. [PubMed: 27478969]

Kung JE, and Jura N. (2019). Prospects for pharmacological targeting of pseudokinases. Nat. Rev. Drug Discov. 18, 501–526. [PubMed: 30850748]

Lemmon MA, and Schlessinger J. (2010). Cell signaling by receptor tyrosine kinases. Cell 141, 1117–1134. [PubMed: 20602996]

Liang LY, Patel O, Janes PW, Murphy JM, and Lucet IS (2019). Eph receptor signalling: from catalytic to non-catalytic functions. Oncogene 38, 6567–6584. [PubMed: 31406248]

Littlefield P, Liu L, Mysore V, Shan Y, Shaw DE, and Jura N. (2014). Structural analysis of the EGFR/ HER3 heterodimer reveals the molecular basis for activating HER3 mutations. Sci. Signal. 7, ra114. [PubMed: 25468994]

Liu X, Pu W, He H, Fan X, Zheng Y, Zhou JK, Ma R, He J, Zheng Y, Wu K, et al. (2019). Novel ROR1 inhibitor ARI-1 suppresses the development of non-small cell lung cancer. Cancer Lett. 458, 76–85. [PubMed: 31125641]

Loving HS, and Underbakke ES (2019). Conformational dynamics of FERM-mediated autoinhibition in Pyk2 tyrosine kinase. Biochemistry 58, 3767–3776. [PubMed: 31403288]

Manning G, Whyte DB, Martinez R, Hunter T, and Sudarsanam S. (2002). The protein kinase complement of the human genome. Science 298, 1912–1934. [PubMed: 12471243]

Martinez Molina D, Jafari R, Ignatushchenko M, Seki T, Larsson EA, Dan C, Sreekumar L, Cao Y, and Nordlund P. (2013). Monitoring drug target engagement in cells and tissues using the cellular thermal shift assay. Science 341, 84–87. [PubMed: 23828940]

Masson GR, Burke JE, Ahn NG, Anand GS, Borchers C, Brier S, Bou-Assaf GM, Engen JR, Englander SW, Faber J, et al. (2019). Recommendations for performing, interpreting and reporting hydrogen deuterium exchange mass spectrometry (HDX-MS) experiments. Nature Methods 16, 595–602. [PubMed: 31249422]

McKinney W. (2010). Data structures for statistical computing in Python. Proceedings of the 9th Python in Science Conference, 51–56.

Mendrola JM, Shi F, Park JH, and Lemmon MA (2013). Receptor tyrosine kinases with intracellular pseudokinase domains. Biochem. Soc.Trans. 41, 1029–1036. [PubMed: 23863174]

Modi V, and Dunbrack RL Jr. (2019). Defining a new nomenclature for the structures of active and inactive kinases. Proc. Natl. Acad. Sci. U. S. A. 116, 6818–6827. [PubMed: 30867294]

Moslin R, Zhang Y, Wrobleski ST, Lin S, Mertzman M, Spergel S, Tokarski JS, Strnad J, Gillooly K, McIntyre KW, et al. (2019). Identification of N-methyl nicotinamide and N-methyl pyridazine-3-carboxamide pseudokinase domain ligands as highly selective allosteric inhibitors of tyrosine kinase 2 (TYK2. J. Med. Chem. 62, 8953–8972. [PubMed: 31314518]

Murphy JM, Zhang Q, Young SN, Reese ML, Bailey FP, Eyers PA, Ungureanu D, Hammaren H, Silvennoinen O, Varghese LN, et al. (2014). A robust methodology to subclassify pseudokinases based on their nucleotide-binding properties. Biochem. J. 457, 323–334. [PubMed: 24107129]

Nagano K, Maeda Y, Kanasaki S, Watanabe T, Yamashita T, Inoue M, Higashisaka K, Yoshioka Y, Abe Y, Mukai Y, et al. (2014). Ephrin receptor A10 is a promising drug target potentially useful for breast cancers including triple negative breast cancers. J. Control. Release 189, 72–79. [PubMed: 24946238]

Novotny CJ, Pollari S, Park JH, Lemmon MA, Shen W, and Shokat KM (2016). Overcoming resistance to HER2 inhibitors through state-specific kinase binding. Nat. Chem. Biol. 12, 923–930. [PubMed: 27595329]

O'Hare T, Shakespeare WC, Zhu X, Eide CA, Rivera VM, Wang F, Adrian LT, Zhou T, Huang WS, Xu Q, et al. (2009). AP24534, a pan-BCR-ABL inhibitor for chronic myeloid leukemia, potently inhibits the T315I mutant and overcomes mutation-based resistance. Cancer Cell 16, 401–412. [PubMed: 19878872]

Overman RC, Debreczeni JE, Truman CM, McAlister MS, and Attwood TK (2014). Completing the structural family portrait of the human EphB tyrosine kinase domains. Protein Sci. 23, 627–638. [PubMed: 24677421]

Patel O, Griffin MDW, Panjikar S, Dai W, Ma X, Chan H, Zheng C, Kropp A, Murphy JM, Daly RJ, et al. (2017). Structure of SgK223 pseudokinase reveals novel mechanisms of homotypic and heterotypic association. Nat. Commun. 8, 1157. [PubMed: 29079850]

Peradziriyi H, Tolwinski NS, and Borchers A. (2012). The many roles of PTK7: a versatile regulator of cell-cell communication. Arch. Biochem. Biophys. 524, 71–76. [PubMed: 22230326]

Petrie EJ, Czabotar PE, and Murphy JM (2019). The structural basis of necroptotic cell death signaling. Trends Biochem. Sci. 44, 53–63. [PubMed: 30509860]

Prebet T, Lhoumeau AC, Arnoulet C, Aulas A, Marchetto S, Audebert S, Puppo F, Chabannon C, Sainty D, Santoni MJ, et al. (2010). The cell polarity PTK7 receptor acts as a modulator of the chemotherapeutic response in acute myeloid leukemia and impairs clinical outcome. Blood 116, 2315–2323. [PubMed: 20558616]

Reiterer V, Eyers PA, and Farhan H. (2014). Day of the dead: pseudokinases and pseudophosphatases in physiology and disease. Trends Cell Biol. 24, 489–505. [PubMed: 24818526]

Ren X, Pan X, Zhang Z, Wang D, Lu X, Li Y, Wen D, Long H, Luo J, Feng Y, et al. (2013). Identification of GZD824 as an orally bioavailable inhibitor that targets phosphorylated and nonphosphorylated breakpoint cluster region-Abelson (Bcr-Abl) kinase and overcomes clinically acquired mutation-induced resistance against imatinib. J. Med. Chem. 56, 879–894. [PubMed: 23301703]

Scheeff ED, Eswaran J, Bunkoczi G, Knapp S, and Manning G. (2009). Structure of the pseudokinase VRK3 reveals a degraded catalytic site, a highly conserved kinase fold, and a putative regulatory binding site. Structure 17, 128–138. [PubMed: 19141289]

Shan Y, Gnanasambandan K, Ungureanu D, Kim ET, Hammarén H, Yamashita K, Silvennoinen O, Shaw DE, and Hubbard SR (2014). Molecular basis for pseudokinase-dependent autoinhibition of JAK2 tyrosine kinase. Nat. Struct. Mol. Biol. 21, 579–584. [PubMed: 24918548]

Shi F. (2012). Ph.D. Thesis: Signaling by non-canonical receptor tyrosine kinases ERBB3 and RYK, (University of Pennsylvania). https://repository.upenn.edu/edissertations/699

Shi F, Telesco SE, Liu Y, Radhakrishnan R, and Lemmon MA (2010). ErbB3/HER3 intracellular domain is competent to bind ATP and catalyze autophosphorylation. Proc. Natl. Acad. Sci. U. S. A. 107, 7692–7697. [PubMed: 20351256]

Shi Z, Resing KA, and Ahn NG (2006). Networks for the allosteric control of protein kinases. Curr. Opin. Struct. Biol. 16, 686–692. [PubMed: 17085044]

Sours KM, Kwok SC, Rachidi T, Lee T, Ring A, Hoofnagle AN, Resing KA, and Ahn NG (2008). Hydrogen-exchange mass spectrometry reveals activation-induced changes in the conformational mobility of p38alpha MAP kinase. J. Mol. Biol. 379, 1075–1093. [PubMed: 18501927]

Steinkamp MP, Low-Nam ST, Yang S, Lidke KA, Lidke DS, and Wilson BS (2014). erbB3 is an active tyrosine kinase capable of homo- and heterointeractions. Mol. Cell. Biol. 34, 965–977. [PubMed: 24379439]

Stricker S, Rauschenberger V, and Schambony A. (2017). ROR-family receptor tyrosine kinases. Curr. Top. Dev. Biol. 123, 105–142. [PubMed: 28236965]

Till JH, Ablooglu AJ, Frankel M, Bishop SM, Kohanski RA, and Hubbard SR (2001). Crystallographic and solution studies of an activation loop mutant of the insulin receptor tyrosine kinase: insights into kinase mechanism. J. Biol. Chem. 276, 10049–10055. [PubMed: 11124964]

Till JH, Becerra M, Watty A, Lu Y, Ma Y, Neubert TA, Burden SJ, and Hubbard SR (2002). Crystal structure of the MuSK tyrosine kinase: insights into receptor autoregulation. Structure 10, 1187–1196. [PubMed: 12220490]

Tsutsui Y, Deredge D, Wintrode PL, and Hays FA (2016). Imatinib binding to human c-Src is coupled to inter-domain allostery and suggests a novel kinase inhibition strategy. Sci. Rep. 6, 30832. [PubMed: 27480221]

Warmuth M, Kim S, Gu XJ, Xia G, and Adrián F. (2007). Ba/F3 cells and their use in kinase drug discovery. Curr. Opin. Oncol. 19, 55–60. [PubMed: 17133113]

Waskom M, Olga B, O'Kane D, Hobson P, Ostblom J, Lukauskas S, Gemperline DC, Augspurger T, Halchenko Y, Cole JB, et al. (2018). 10.5281/zenodo.1313201.

Winter G, Lobley CM, and Prince SM (2013). Decision making in xia2. Acta Crystallogr. D. Biol. Crystallogr. 69(Pt 7), 1260–1273. [PubMed: 23793152]

Wroblewski ST, Moslin R, Lin S, Zhang Y, Spergel S, Kempson J, Tokarski JS, Strnad J, Zupa-Fernandez A, Cheng L, et al. (2019). Highly selective inhibition of tyrosine kinase 2 (TYK2) for the treatment of autoimmune diseases: Discovery of the allosteric inhibitor BMS-986165. J. Med. Chem. 62, 8973–8995. [PubMed: 31318208]

Wybenga-Groot LE, Baskin B, Ong SH, Tong J, Pawson T, and Sicheri F. (2001). Structural basis for autoinhibition of the Ephb2 receptor tyrosine kinase by the unphosphorylated juxtamembrane region. Cell 106, 745–757. [PubMed: 11572780]

Xie T, Lim SM, Westover KD, Dodge ME, Ercan D, Ficarro SB, Udayakumar D, Gurbani D, Tae HS, Riddle SM, et al. (2014). Pharmacological targeting of the pseudokinase Her3. Nat. Chem. Biol. 10, 1006–1012. [PubMed: 25326665]

Yamaguchi T, Yanagisawa K, Sugiyama R, Hosono Y, Shimada Y, Arima C, Kato S, Tomida S, Suzuki M, Osada H, et al. (2012). NKX2–1/TITF1/TTF-1-induced ROR1 is required to sustain EGFR survival signaling in lung adenocarcinoma. Cancer Cell 21, 348–361. [PubMed: 22439932]

Zeqiraj E, Filippi BM, Goldie S, Navratilova I, Boudeau J, Deak M, Alessi DR, and van Aalten DM (2009). ATP and MO25alpha regulate the conformational state of the STRADalpha pseudokinase and activation of the LKB1 tumour suppressor. PLoS Biol. 7, e1000126.

Zeqiraj E, and van Aalten DM (2010). Pseudokinases-remnants of evolution or key allosteric regulators? Curr. Opin. Struct. Biol. 20, 772–781. [PubMed: 21074407]

Zhang S, Zhang H, Ghia EM, Huang J, Wu L, Zhang J, Lam S, Lei Y, He J, Cui B, et al. (2019). Inhibition of chemotherapy resistant breast cancer stem cells by a ROR1 specific antibody. Proc. Natl. Acad. Sci. U. S. A. 116, 1370–1377. [PubMed: 30622177]

HIGHLIGHTS

- Pseudokinases share autoinhibitory interactions of their closest kinase relatives

- Structural dynamics of pseudokinases closely resemble those of canonical kinases

- ROR1 ATP-binding site can be targeted with small molecules despite being occluded

- Inhibitor binding disrupts pseudokinase conformation and may inhibit signaling
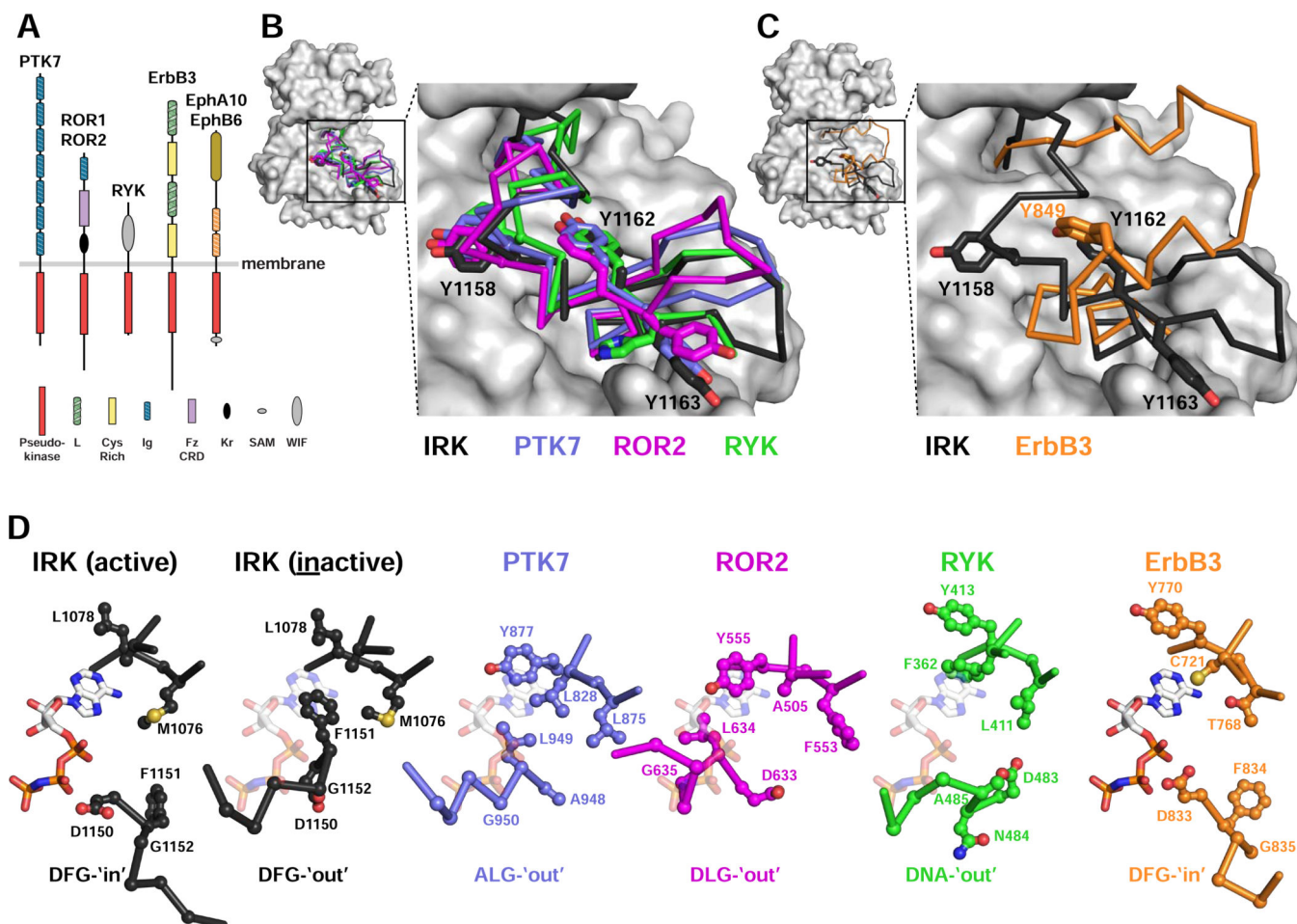
FIGURE 1. Pseudokinases retain autoinhibitory interactions of the insulin receptor

(**A**) Domain composition of human RTK pseudokinases, with the extracellular region above, and intracellular region below the membrane. Domains are listed in the legend: pseudokinase (red), leucine-rich (L), cysteine-rich (Cys Rich), immunoglobulin (Ig), Frizzled cysteine-rich domain (Fz CRD), Kringle domain (Kr), Sterile Alpha Motif (SAM), and Wnt Inhibitory Factor (WIF) domain

(**B**) Activation loops of pseudokinase domains from PTK7 (slate blue), ROR2 (magenta), and RYK (green) are superimposed on that of IRK (black) in the context of the IRK surface (from PDB: 1IRK). YxxxYY tyrosines in IRK are labeled. The ROR2 structure is chain B of PDB: 3ZZW.

(**C**) ErbB3 activation loop structure (Littlefield et al., 2014) from PDB: 4RIW, superimposed on the 1IRK surface as in (B), with ErbB3 colored orange. Y849 is labelled.

(**D**) Close-up of residues surrounding the ATP binding site for active and inactive IRK (black), PTK7, ROR2, RYK, and ErbB3, colored as above. AMP-PNP is solid when seen in the relevant crystal structure and transparent when not. Residues from the DFG motif (and 4 residues beyond), the β5/αD hinge, and second residue of the VAIK motif are shown (VAVK in IRK, VLVK in PTK7, VAIK in ROR2, AFVK in RYK, VCIK in ErbB3).
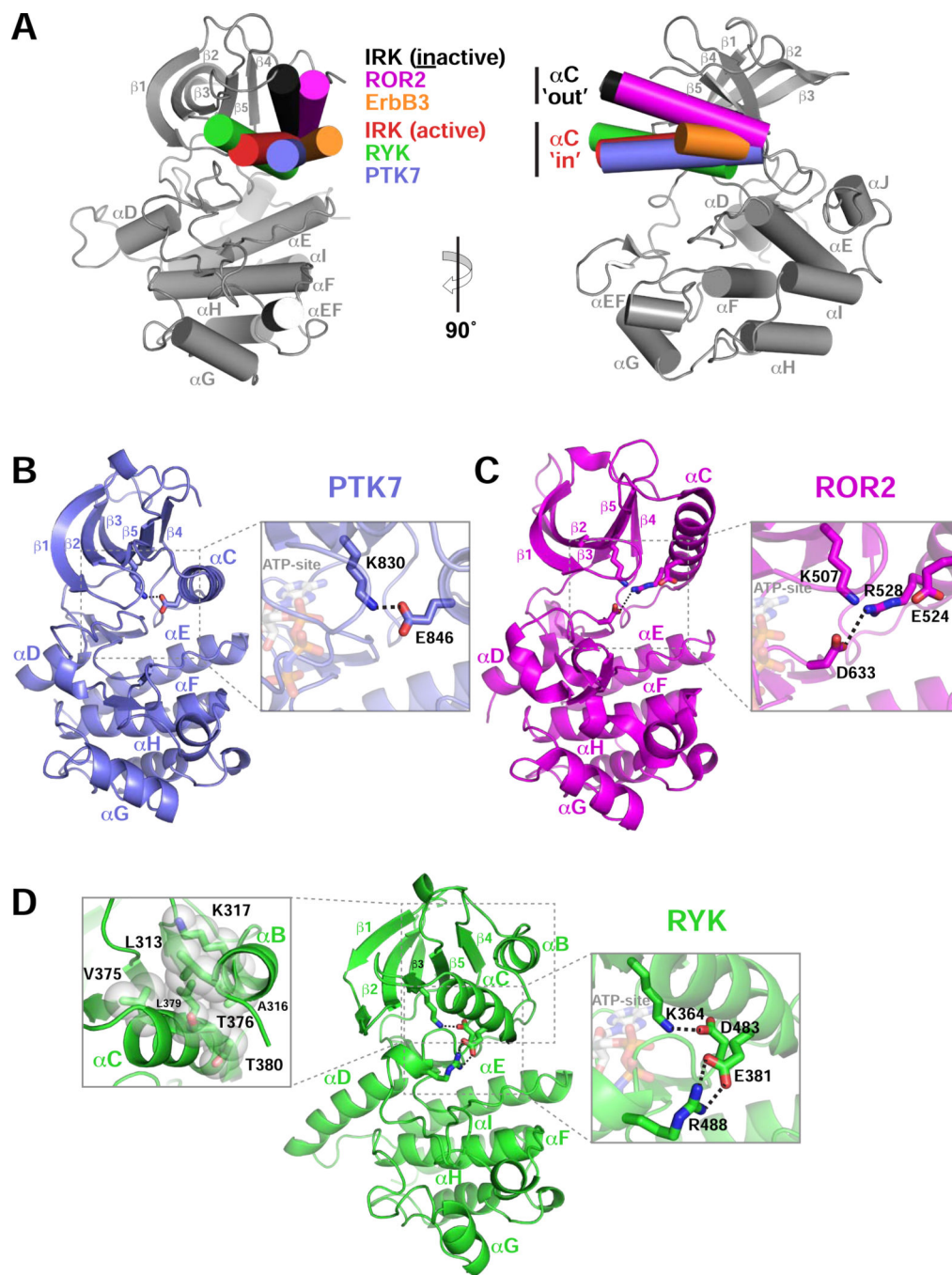
See also Figure S1 and Table 1.

FIGURE 2. Overall structure of pseudokinase domains

(**A**) Cartoon representing pseudokinase αC helix positions. Two orthogonal views of inactive IRK (1IRK) are shown in grey. Helix αC of IRK, which adopts the 'out' position is colored black. Helix αC from ROR2 (3ZZW; magenta) and ErbB3 (4RIW; orange) is also 'out'. By contrast, αC is 'in' for PTK7 (slate blue), RYK (green), and active IRK (1IR3). (**B**) PTK7 pseudokinase domain. The insert shows the predicted salt bridge between the αC glutamate (E846) and β3 lysine (K830).

(**C**) ROR2 pseudokinase domain (chain B from 3ZZW). Insert shows absence of salt bridge between the αC glutamate (E524) and β3 lysine (K507), and alternate contact between D633 (in the DLG motif) and R528 (in αC).

(**D**) RYK pseudokinase domain. Inserts show hydrophobic side-chains involved in packing between helices αB and αC (left) and connections between the DFG (DNA) motif region and helix αC (right). Interactions between D483 (in DNA motif) and the β3 lysine (K364) and between R488 (close to DNA motif) and αC glutamate (E381) are shown. Vestigial ATP-binding sites are labelled in inserts of (**B-D**) using a transparent AMP-PNP molecule positioned as in active IRK.
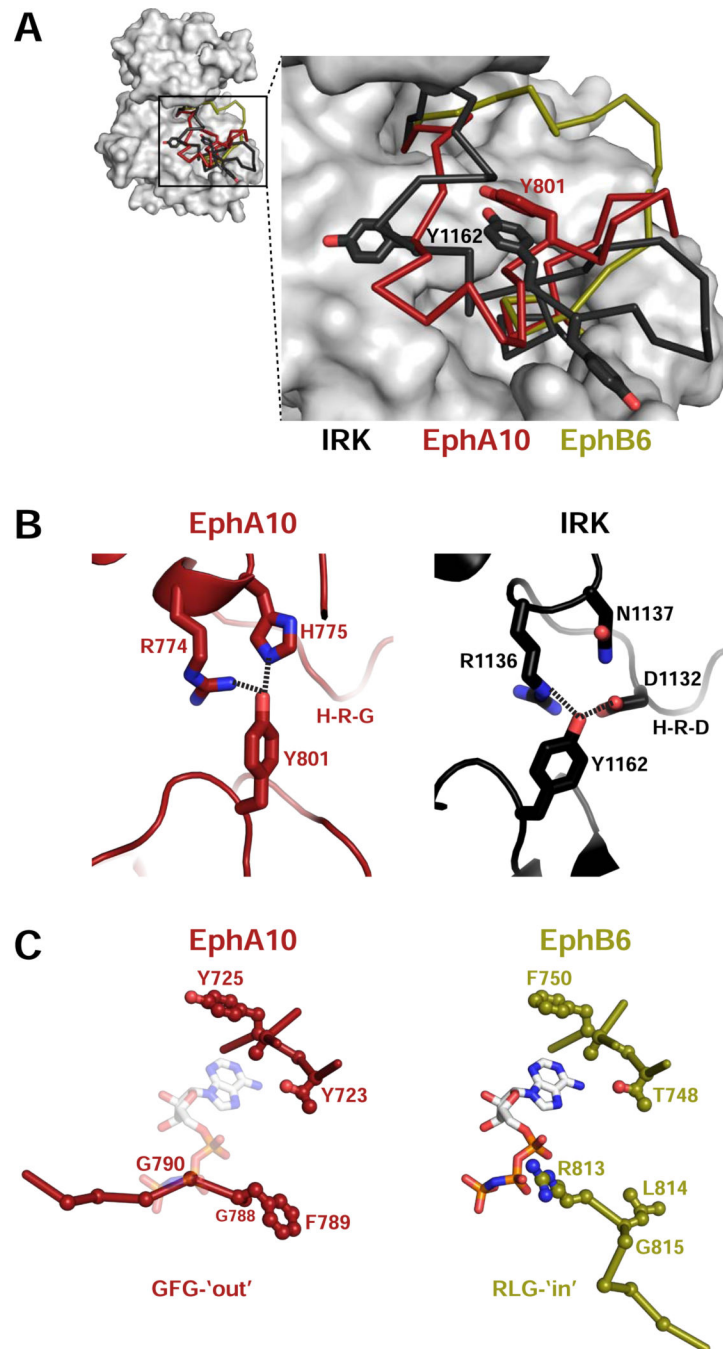
See also Figure S2.

FIGURE 3. Insights into EphA10 and EphB6 pseudokinases from modeling

(**A**) Activation loops in models of the EphA10 (deep red) and EphB6 (olive) pseudokinases, superimposed on that of IRK (black) in the context of the IRK surface (from PDB: 1IRK). Y1162 in IRK and its EphA10 equivalent (Y801) are labeled.

(**B**) Close-up of interactions involving Y801 for EphA10 (left) and Y1162 for IRK (right). Where Y1162 of IRK interacts with D1132 in the HRD motif and R1136 from the end of the catalytic loop, in EphA10 Y801 retains the arginine interaction (with R774), but interacts

with a histidine at the very end of the catalytic loop (H775) making up for the lack of an HRD aspartate (replaced by glycine in EphA10).

(**C**) Close-up of residues around the ATP binding sites of EphA10 (left), and EphB6 (right), colored as above. An AMP-PNP molecule is shown – solid when predicted to bind and transparent when not. Residues are shown from the DFG motif (GFG in EphA10, and RLG in EphB6) – and 4 residues beyond – as well as the β5/αD hinge.
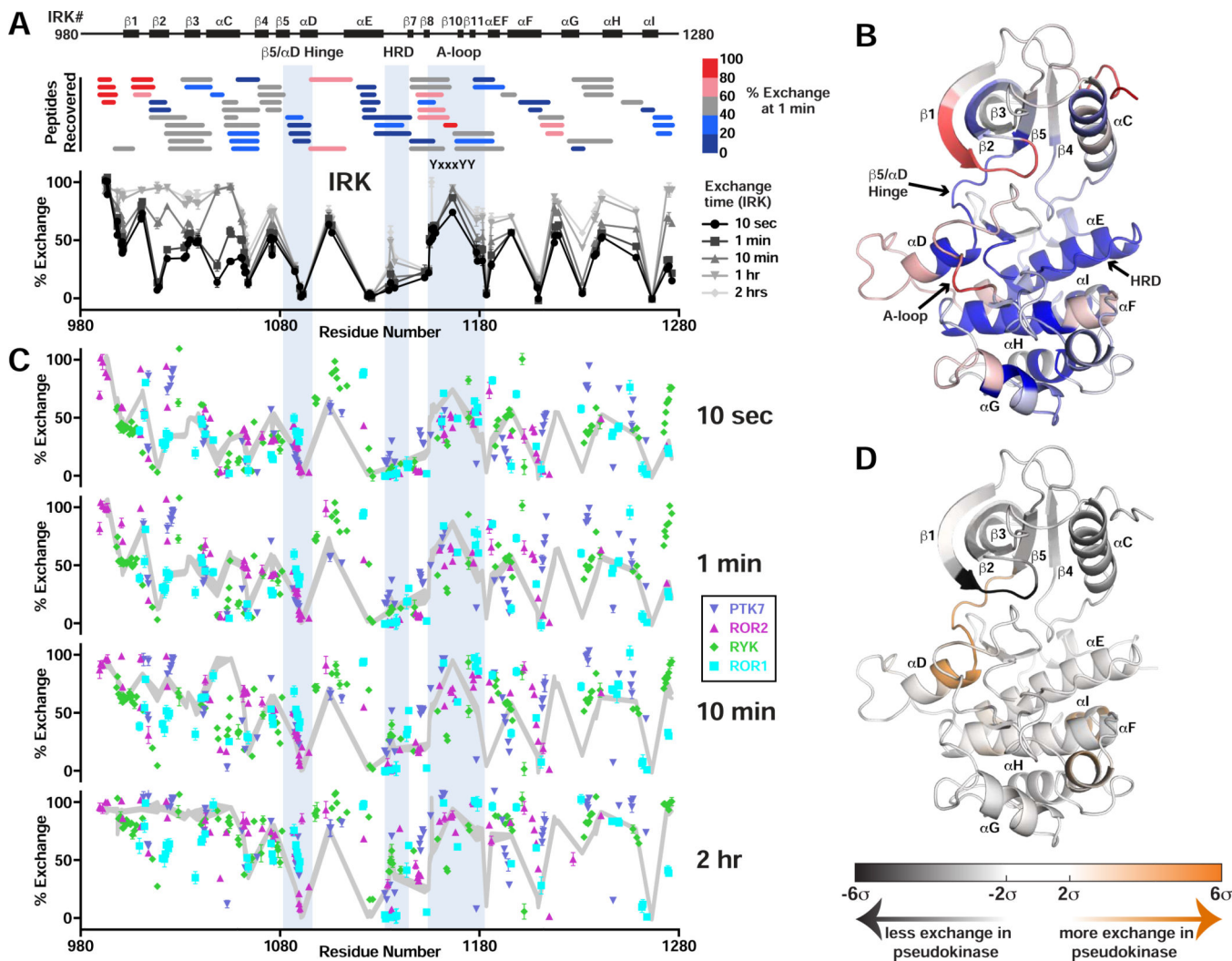
See also Figure S3.

FIGURE 4. Comparison of pseudokinase domain dynamics by HDX

(**A**) HDX data at 1 minute for unphosphorylated IRK across 73 peptides (represented as short horizontal lines). Lines are colored according to percent exchange at 1 min (using the scale at right). Secondary structure of IRK is shown at top. Data for longer timepoints are plotted in the lower part of the figure, with the x-axis representing the median residue number of the peptide. Locations of the β5/αD hinge, HRD motif, activation loop (A-loop) and YxxxYY motif are noted. Errors represent SD from three independent labeling experiments.

(**B**) Data (1 min) from the upper part of (**A**) plotted on the (inactive) IRK structure using the same color scheme as in (**A**). Blue represents less, and red more, exchange.

(**C**) Comparison of HDX data (mean ± SD) for PTK7 (slate blue), ROR2 (magenta), RYK (green) and ROR1 (cyan) pseudokinase domains with data for IRK (grey) at 10 s, 1 min, 10 min, and 2 h. X-axis represents IRK-equivalent median residue number. IRK data are depicted as the range for each point. Errors represent SD from three independent labeling experiments.

(**D**) Variance of 'exchangeability index' values – determined as in STAR Methods – for pseudokinases versus IRK (expressed as how many times SD/σ was the IRK value away from the pseudokinase mean), plotted on the inactive IRK structure. A location was assigned no color if within 2σ, but colored black or orange as marked if beyond 2σ (95% confidence). See also Figure S4 and Table S1.
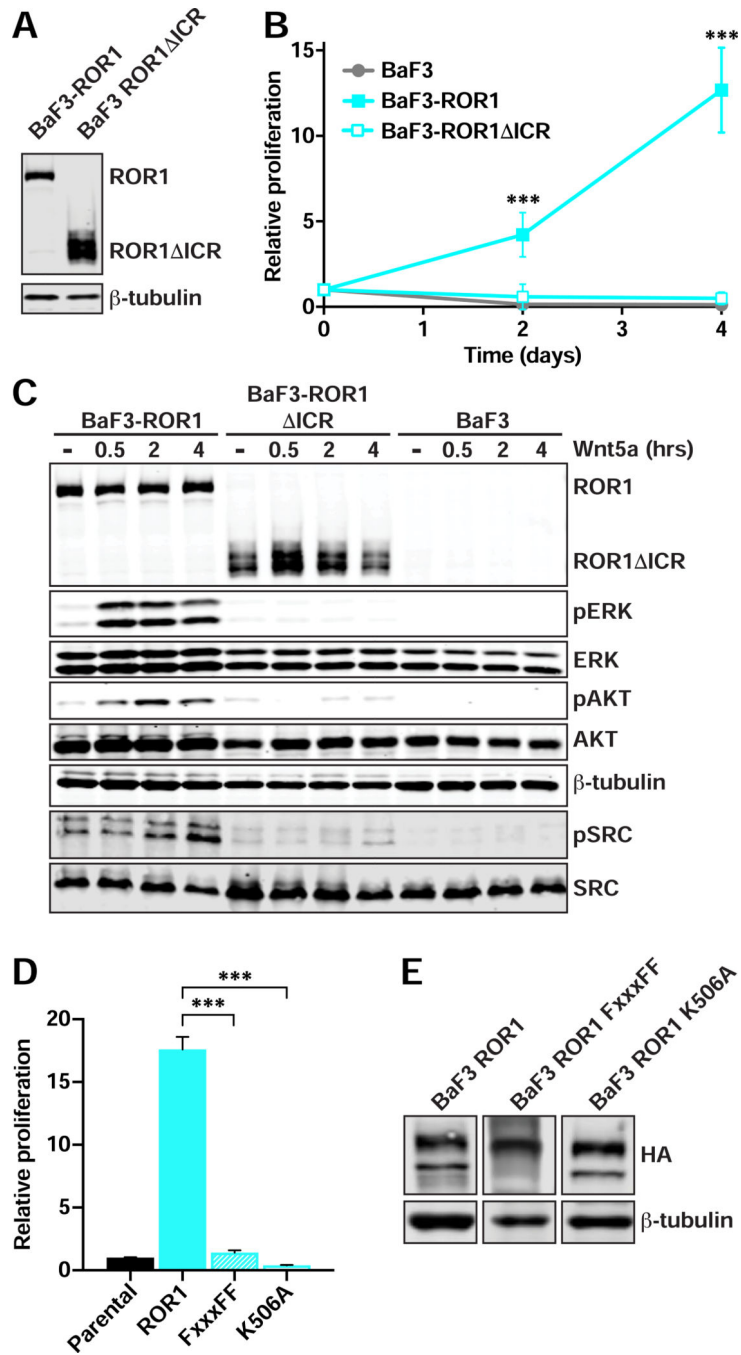
FIGURE 5. ROR1 signaling in BaF3 cells

(**A**) ROR1 and ROR1 ICR expression in BaF3 stable clones by anti-HA Western blot (with β-tubulin as loading control).

(**B**) BaF3 (parental), BaF3-ROR1 and BaF3-ROR1 ICR cells were cultured without IL3 or Wnt5a. Cell number was counted using Trypan-blue exclusion at the indicated time points, and plotted (mean ± SD) for 4 independent experiments. Statistical significance is defined: ***p   0.001; **p   0.01; *p   0.05.

(**C**) BaF3, BaF3-ROR1 and BaF3-ROR1 ICR cells were serum starved overnight, and then treated with recombinant Wnt5a (50 ng/ml) for the indicated times. Cell lysates were immunoblotted with the indicated antibodies. ROR1 or ROR1 ICR protein levels were determined using anti-HA blotting. A representative of three independent experiments is shown.

(**D**) Proliferation of BaF3 cells expressing different ROR1 variants as noted (in the absence of IL3 or Wnt5a), assessed using the CellTiter-Glow 2.0 Assay 14 days after seeding, and expressed as a fold increase over that seen for parental BaF3 cells. Data are represented as mean values ± SD, for 3 biological repeats. ***p 0.001.

(**E**) Assessment of stable BaF3 clones expressing (HA-tagged) wild-type ROR1, a variant with the activation loop YxxxYY motif mutated to FxxxFF (Y641F/Y645F/Y646F), and a K506-Amutated variant by Western blotting with anti-HA and β-tubulin as loading control. See also Figure S5.
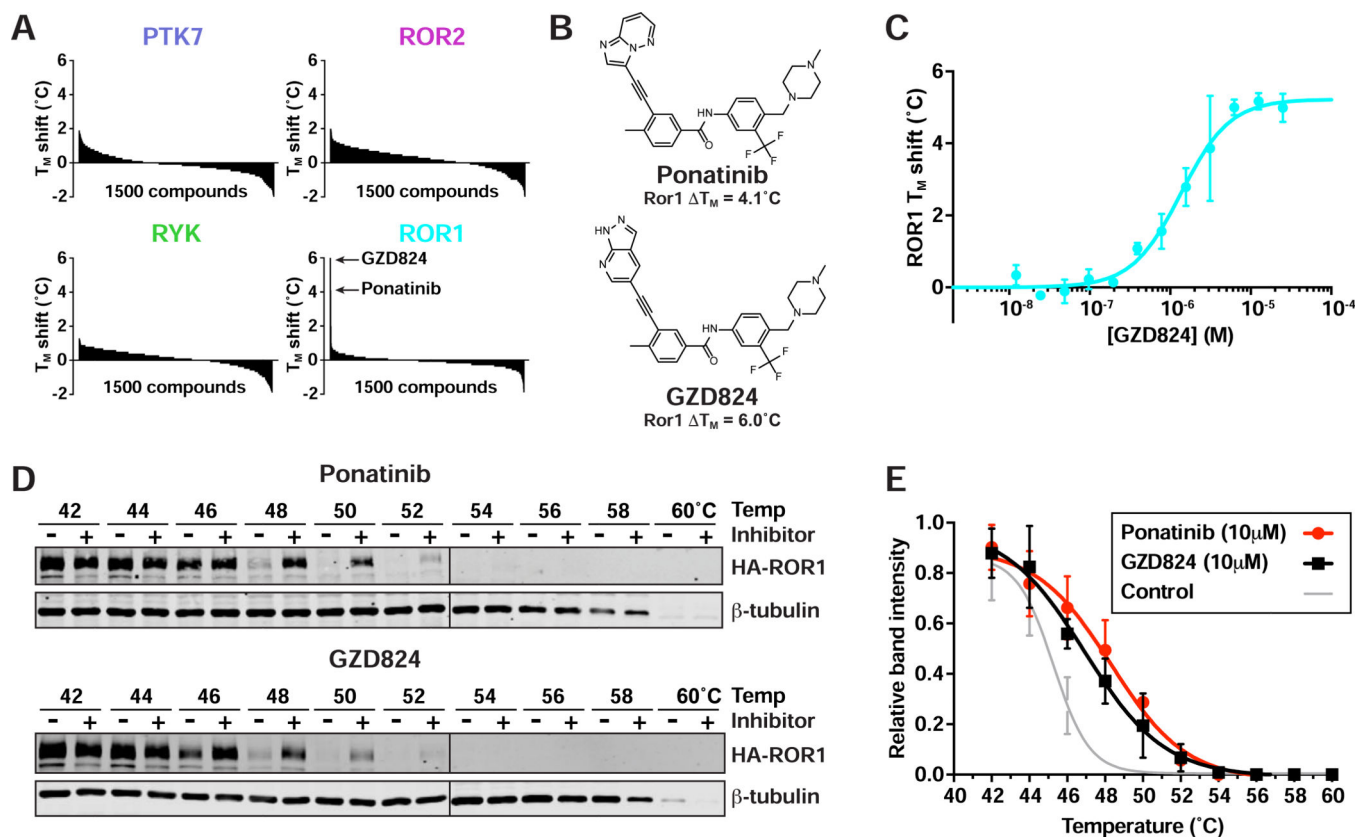
FIGURE 6. Screening for small molecules that bind pseudokinase domains

(**A**) Summary of DSF-based screen for small molecule binders of Wnt-binding RTK pseudokinases. Hits identified in the ROR1 screen are denoted with horizontal arrows. Compounds screened, and screening results, are listed in Table S2.

(**B**) Chemical structures of the two ROR1-binding 'hits' from (**A**).

(**C**) T_M shift as a function of GZD824 concentration binding to purified ROR1 pseudokinase domain (at 2 μM) using DSF, with curve fit as described in STAR Methods. Mean ± SD is shown for three independent experiments.

(**D**) Cellular thermal shift assay (CETSA) showing stabilization of ROR1 in cells upon addition of ponatinib or GZD824. BaF3-ROR1 cells were treated with 10 μM ponatinib or GZD824, and subjected to the noted temperatures as described in STAR Methods. Cell lysates were blotted with anti-HA to assess ROR1 levels, and with anti-β-tubulin as a loading control.

(**E**) CETSA data as in (**D**), derived from signal quantification of 3 independent experiments (mean ± SD), with curves fit as described in STAR Methods. Band intensities were normalized to the non-heated and non-treated sample for each experiment (set at a value of 1). Control (grey) curve represents heated samples without added inhibitor.
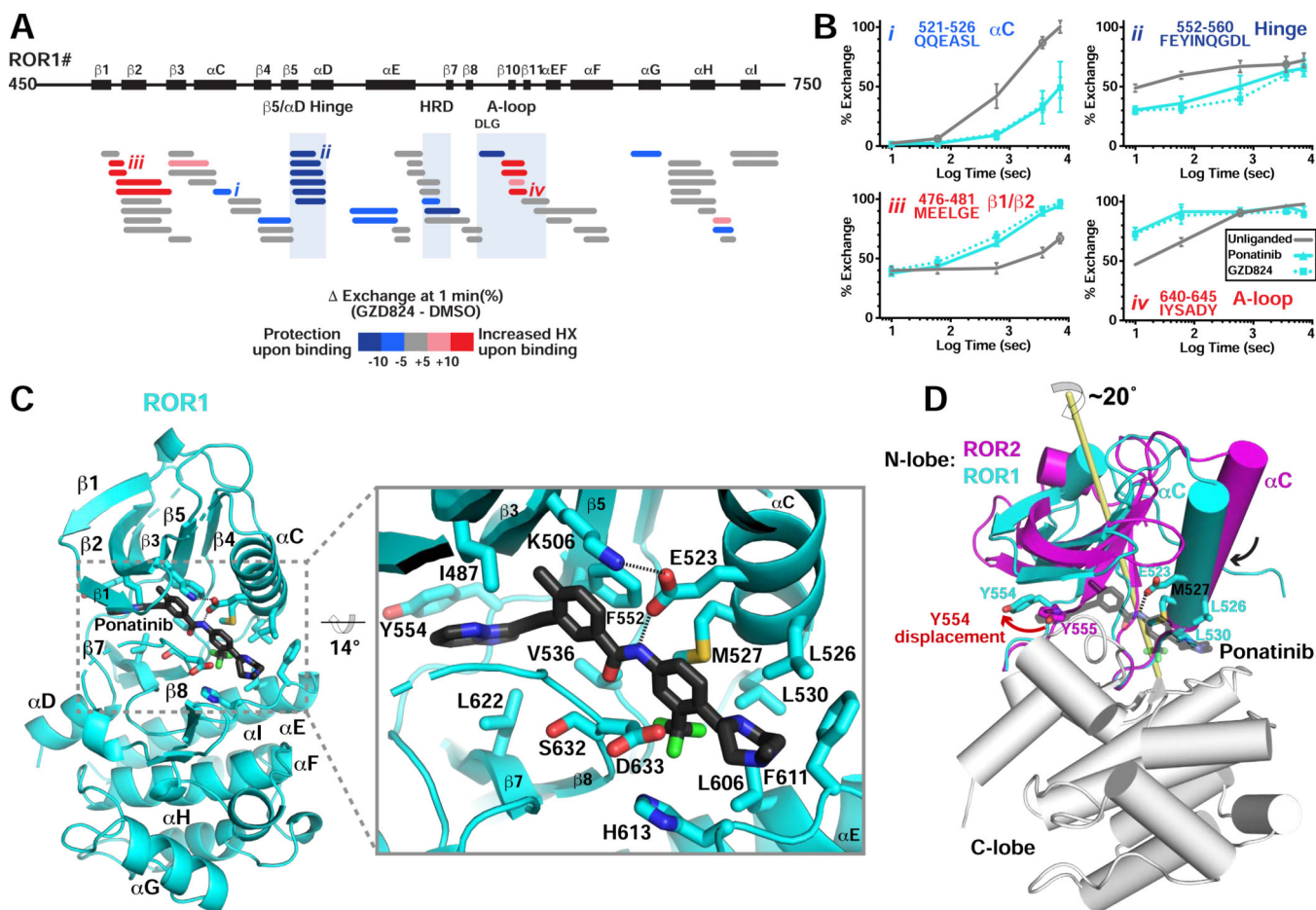
See also Figure S6 and Table S2.

FIGURE 7. Binding of ponatinib and GZD824 to the ROR1 pseudokinase domain

(**A**) HDX data for ROR1, comparing exchange differences for 62 peptides with- and without added GZD824 (50 μM) at a representative 1 min timepoint. Color coding is shown in the scale at bottom, red representing increased HDX upon inhibitor binding, and blue a reduction. Data for selected peptides (*i*, *ii*, *iii*, and *iv*) are detailed in (**B**). ROR1 secondary structure is shown at top. Values for all time points for three biological replicates are shown in Fig. S7A.

(**B**) HDX data for selected peptides showing HDX with- and without inhibitor across 3 biological replicates (mean ± SD). Data are shown for ponatinib treatment (solid cyan line) and GZD824 treatment (dotted cyan line), for peptides marked in (**A**): *i* (from helix αC); *ii* (from β5/αD hinge); *iii* (from β1/β2 loop); and *iv* (from the activation loop).

(**C**) Structure of ponatinib-bound ROR1 pseudokinase, shown in cyan (ponatinib is black), with side-chains involved in ponatinib binding detailed in the zoomed view.

(**D**) Overlay of the ponatinib-bound ROR1 pseudokinase domain on the ROR2 pseudokinase domain, using only the C-lobe to guide overlay. In comparing these structures, DynDom3D (Girdlestone and Hayward, 2016) identified an ~20˚ rotation of the N-lobe with respect to the C-lobe about the yellow near-vertical axis as described in the text. The hinge tyrosine (Y554 in ROR1, Y555 in ROR2) and ROR1 αC helices that interact with ponatinib are labeled, and the displacement of this tyrosine by ponatinib is depicted with a red arrow.

See also Figure S7 and Table S1.

Table 1.

Crystallization Conditions, Data Collection and Refinement Statistics

Protein	PTK7	RYK	ROR1-ponatinib
PBD ID	6VG3	6TUA	6TU9
Crystallization Conditions	11 mg/ml protein, 100 mM ADA (pH 6.5), 100 mM $(NH_4)_2SO_4$, 30% (w/v) PEG monoethyl ether 5000, 20°C	11 mg/ml protein, 100 mM HEPES (pH 7.5), 1.5 M Li_2SO4, 20°C	13 mg/ml protein, 0.5 mM ponatinib, 100 mM MES (pH 7.2), 12% (w/v) PEG 20K, 4°C
Data Collection[a]			
Beamline	APS/NE-CAT 24-ID-C	SLS X06SA	SLS X06SA
Date of collection	June 20, 2017	December 7, 2018	December 7, 2018
Wavelength (Å)	0.979	0.99999	0.99999
Space Group	$C\,2\,2\,2_1$	$I\,2$	$P\,2_1$
Cell Dimensions			
a, b, c (Å)	95.63, 119.92, 166.52	60.64, 47.24, 152.74	54.29, 85.97, 72.98
α, β, γ, (°)	90, 90, 90	90.00, 97.64, 90.00	90.00, 91.05, 90.00
Resolution (Å)	48.7 – 1.95	37.85 – 2.38	39.12 – 1.94
Completeness	98.5 (97.7)	98.3 (96.3)	98.7 (97.5)
Redundancy	8.1 (8.1)	3.7 (3.6)	5.0 (5.0)
R_{sym} (%)	9.2 (102.1)	6.4 (38.6)	5.8 (52.1)
I/σ	13.4 (1.9)	8.3 (2.0)	8.0 (2.0)
$CC^{1/2}$ [b]	0.999 (0.74)	1.0 (0.9)	1.0 (0.8)
Refinement			
Number of reflections	68,916 (9835)	17,213 (1691)	49,066 (4844)
Rwork/Rfree (%)	18.4/22.9	19.4/24.8	20.9/24.1
Number of atoms			
Protein	6516	2270	4000
Ions	0	25	0
Ligands	0	0	78
Water	598	28	94
Average B factor (Å)			
Protein	45.5	40.3	47.9
Ions	-	92.4	-
Ligands	-	-	37.9
Water	36.2	33.9	42.0
Ramachandran favored (%)	96.4	97.6	96.5
Ramachandran allowed (%)	3.6	2.1	3.5
Ramachandran outliers (%)	0.0	0.4	0.0
Bond length rmsd (Å)	0.009	0.008	0.007
Bond angle rmsd (Å)	1.01	0.88	0.84

[a]Numbers in parentheses denote highest resolution shell

bCC$^{1/2}$ reported for the highest resolution shell

KEY RESOURCES TABLE

REAGENT or RESOURCE	SOURCE	IDENTIFIER
Antibodies		
Rabbit monoclonal anti-phosphoAKT S473	Cell Signaling Technology	Cat#: 4060; RRID:AB_2315049
Rabbit polyclonal anti-AKT	Cell Signaling Technology	Cat#: 9272; RRID:AB_329827
Rabbit polyclonal anti-phospho-p44/42 (ERK1/2, Thr202/Thr204)	Cell Signaling Technology	Cat#: 9101; RRID:AB_331646
Mouse monoclonal anti-ERK1/2	Cell Signaling Technology	Cat#: 4696; RRID:AB_390780
Rabbit monoclonal anti-SRC	Cell Signaling Technology	Cat#: 36D10
Mouse monoclonal anti-Phospho-Tyrosine 4G10	Merck Millipore	Cat#: 05–321
Rabbit monoclonal anti-Wnt5a/b	Cell Signaling Technology	Cat#: 2530; RRID:AB_2215595
Rabbit monoclonal anti-PTK7/CCK4	Cell Signaling Technology	Cat#: 25618; RRID:AB_2798907
Mouse monoclonal anti-ROR1 4A5	BD Biosciences	Cat#: 564464; RRID:AB_2738817
Mouse monoclonal anti-ROR2	BD Biosciences	Cat#: 565550; RRID:AB_2739291
Mouse monoclonal β-tubulin	Santa Cruz Biotechnology	Cat#: sc-166729; RRID:AB_2010699
Mouse monoclonal anti-HA.11 epitope tag	BioLegend	Cat#: 901513; RRID:AB_2565335
IRDye 680RD Donkey anti-Rabbit IgG	LI-COR Biosciences	Cat#: 926–68073, RRID:AB_10954442
IRDye 800CW Donkey anti-Mouse IgG	LI-COR Biosciences	Cat#: 926–32212, RRID:AB_621847
Bacterial and Virus Strains		
Baculovirus shuttle vector bMON14272	Invitrogen	10359–016
Chemicals, Peptides, and Recombinant Proteins		
Recombinant human/mouse Wnt5a	Bio-Techne (R&D)	Cat#: 645-WN-010; #P22725
cOmplete, mini, EDTA-free Protease Inhibitor Cocktail	Sigma-Aldrich/Roche	Cat#: 11836170001
Ponatinib	Selleck Chemicals	Cat#: S1490; CAS:943319–70-8
GZD824 Dimesylate	Selleck Chemicals	Cat#: S7194; CAS:1421783–64-3
Kinase Inhibitor Library	Selleck Chemicals	Cat#: L1200
FDA-approved Drug Library	Selleck Chemicals	Cat#: L1300
SYPRO Orange Protein Gel Stain	ThermoFisher Scientific	Cat#: S6650
SYPRO Orange Protein Gel Stain	Millipore Sigma	Cat#: S5692
Deuterium Oxide (99.9%) Low paramagnetic	Cambridge Isotope Labs	Cat#: DLM-11–100
Guanidine:DCl (98%)	Cambridge Isotope Labs	Cat#: DLM-1846–1
Poly(Glu, Tyr) sodium salt (4:1)	Sigma-Aldrich	Cat#: P0275
Sox-based Kinase Activity Peptide Sensor	Assay Quant Technologies	AQT0001
Critical Commercial Assays		
SF Cell Line 4D-Nucleofector X Kit L	Lonza	V4XC-2012
CellTiter-Glo 2.0 Cell Viability assay	Promega	G9243
ADP-Glo Kinase Assay	Promega	V6930
Deposited Data		
PTK7 crystal structure	This manuscript	6VG3

REAGENT or RESOURCE	SOURCE	IDENTIFIER
RYK crystal structure	This manuscript	6TUA
ROR1-ponatinib crystal structure	This manuscript	6TU9
Experimental Models: Cell Lines		
Mouse: *M. musculus* BaF3 pro B cells	DSMZ	ACC 300
Insect: *S. frugiperda* Sf9 cells	Expression Systems	Cat#: 94–001F
Insect: *S. frugiperda* TriEx Sf9 cells	Novagen	Cat#: 71023–3
Recombinant DNA		
pEFIRES-puromycin	(Hobbs et al., 1998)	N/A
pEFIRES-ROR1-HA	This manuscript	N/A
pEFIRES-ROR1 ICR-HA (473–937)	This manuscript	N/A
pEFIRES-ROR2-HA	This manuscript	N/A
pEFIRES-PTK7-HA	This manuscript	N/A
pFastbac1	Invitrogen	Cat#: 10360014
pFastbac1–6xHis-PTK7$^{774-1069}$	This manuscript	N/A
pFastbac-6HZD-ROR1$^{453-752}$	This manuscript	N/A
pFastbac1–6xHis-ROR1$^{457-752}$	This manuscript	N/A
pFastbac1–6xHis-ROR2$^{452-753}$	(Artim et al., 2012)	N/A
pFastbac1-IRK$^{1005-1310}$	(Hubbard et al., 1994)	N/A
pFastbac1–6xHis-IRK$^{1005-1310}$	This manuscript	N/A
pFastbac-6HZD-RYK$^{292-607}$	This manuscript	N/A
pFastbac1–6xHis-TEV-RYK$^{318-607}$	This manuscript	N/A
Software and Algorithms		
Pandas	(McKinney, 2010)	https://pandas.pydata.org/
Seaborn	(Waskom et al., 2018)	https://seaborn.pydata.org/
Matplotlib	(Hunter, 2007)	https://matplotlib.org/
GraphPad Prism 7	GraphPad Software, La Jolla California USA	www.graphpad.com
Coot	(Emsley and Cowtan, 2004)	Version 0.8.7 http://www2.mrc-lmb.cam.ac.uk/personal/pemsley/coot
CCP4i	(CCP4, 1994)	Version 7.0.053
PyMol	Schrödinger	www.pymol.org
PHENIX	(Adams et al., 2010)	https://www.phenix-online.org
Image Studio Lite	LI-COR	https://www.licor.com/bio/image-studio-lite/
MassLynx	Waters	Version 4.2
ProteinLynx Global Server	Waters	Version 3.0.3
DynamX	Waters	Version 3.0
RStudio	RStudio, Inc.	Version 1.2.5001
DynDom3D	(Girdlestone and Hayward, 2016)	http://dyndom.cmp.uea.ac.uk/dyndom/